Large eddy simulation of stratified flow past prolate spheroids with varying aspect ratios ⊘

Gang Gao (高港) (iD) ; Yangjun Wang (汪杨骏); Kefeng Liu (刘科峰); Liushuai Cao (曹留帅) ✉ (iD) ;
Decheng Wan (万德成) (iD)

Check for updates

View Online

Export Citation

Articles You May Be Interested In

KoopmanLab: Machine learning for solving complex physics equations

APL Mach. Learn. (September 2023)

Experimental realization of a quantum classification: Bell state measurement via machine learning

APL Mach. Learn. (September 2023)

Large eddy simulation of stratified flow past prolate spheroids with varying aspect ratios

Gang Gao (高港),[1] [ID] Yangjun Wang (汪杨骏),[2] Kefeng Liu (刘科峰),[2] Liushuai Cao (曹留帅),[1,a] [ID]
and Decheng Wan (万德成)[1] [ID]

AFFILIATIONS

[1]Computational Marine Hydrodynamics Lab (CMHL), School of Ocean and Civil Engineering, Shanghai Jiao Tong University, Shanghai 200240, China

[2]College of Advanced Interdisciplinary Studies, National University of Defense Technology, Nanjing 210022, China

Note: This paper is part of the Special Topic, Recent Advances in Fluid Dynamics and Its Applications.
a)Author to whom correspondence should be addressed: liushuaicao@sjtu.edu.cn

ABSTRACT

This study employs large eddy simulation and the Boussinesq approximation to investigate the characteristics of wakes generated by prolate spheroid with different aspect ratios (length-to-diameter ratios, $L/D = 1.0, 1.5, 2.0, 3.0$) in a linear stratified flow, with the Reynolds number (Re) of 3700 and the Froude number (Fr) of 3. The research primarily focuses on the effects of different aspect ratios on defect velocity, wake length scales, root mean square values of velocity components, power spectra, wake energy, and turbulent kinetic energy (TKE). The findings show that the defect velocity along the wake centerline follows the relationships: $u \sim (x/D)^{-0.08}$ ($L/D = 1.0$), as the aspect ratio increases, the exponent gradually decreases, indicating a shorter mean lifespan of the wake. After the starting position of the accelerated collapse stage, the half-width, half-height, the ratio of half-height to half-width, and the influence area of the wake oscillate periodically. With the aspect ratio increases, the half-width, half-height, the ratio of half-height to half-width, and the influence area of the wake are gradually becoming smaller, and the Reynolds stress gradually decreases in magnitude and becomes concentrated near the centerline of the wake. The turbulent kinetic energy for different aspect ratios follows the relationship TKE $\sim (x/D)^{-1.19}$. The mean kinetic energy, turbulent kinetic energy, and turbulent potential energy (TPE) of the wake all decrease with increasing aspect ratio. Both the energy of wake and transport, advection, and buoyancy terms in turbulent kinetic energy budget exhibit periodic oscillations, with the oscillation wavelength corresponding to half a buoyancy period ($\pi \cdot Fr$). All terms in turbulent kinetic energy budget decrease with the aspect ratio increases.

I. INTRODUCTION

Stratified flow is a prevalent phenomenon observed in natural environments. Solar ponds and reservoirs exhibit temperature stratification due to solar radiation, with higher temperatures near the free surface and lower temperatures underwater.[1,2] In seawater, salinity stratification occurs alongside temperature stratification as salinity varies with depth. Density stratification in seawater arises from the combined effects of temperature and salinity.[3,4]

When an object moves through a fluid, it generates a wake. The Reynolds number (Re), a dimensionless parameter governing wake, is expressed as

$$Re = \frac{UD}{\nu}, \tag{1}$$

where U, D, and ν denote the incoming flow velocity, characteristic length scale, and kinematic viscosity, respectively.

The internal Froude number (Fr), a dimensionless parameter, quantifies the strength of stratified flow and is expressed as

$$Fr = \frac{U}{ND}, \tag{2}$$

where N represents the buoyancy frequency, defined as

$$N = \sqrt{-\frac{g}{\rho_0}\frac{d\rho}{dz}}, \tag{3}$$

where g, ρ_0, ρ, and z denote gravitational acceleration, reference density, density, and vertical coordinate, respectively.

Two dimensionless parameters characterize time and distance

$$Nt = N \cdot t, \tag{4}$$

where t represents the characteristic timescale. Nt is defined using the timescale, with the period of buoyancy oscillation serving as the

fundamental time unit. It is primarily used to study the temporal evolution of wake

$$Nt = \frac{x}{FrD}, \tag{5}$$

where x represents various positions within the wake region. Nt is defined using the distance scale, incorporating stratification strength and spatial scale, and is primarily employed to describe the spatial evolution of the wake.

Current research on wake dynamics primarily focuses on two approaches: experimental studies and numerical simulations. For uniform flow, Kim and Durbin[5] measured the vortex shedding frequency in wake flows using hot-film probes and flow visualization techniques in wind tunnel experiments. They observed that in natural wake flows, the Strouhal number (St) equals 0.2. When the excitation frequency nears the natural vortex shedding frequency, the wake structure is significantly enhanced, whereas it is suppressed when the frequency deviates. In stratified flow experiments, researchers primarily employed dye-tracing methods, laser-induced fluorescence and particle image velocimetry. Lin et al.[6] found in linear stratified flow experiments that the maximum vertical thickness (S_{max}/D) of the wake follows $S_{max}/D \sim Fr$ ($Fr \leq 2.0$) and $S_{max}/D \sim Fr^{1/3}$ ($Fr > 2.0$). The horizontal wake evolution follows $y/D \sim t^{1/3}$, transitioning to $y/D \sim t^{1/2}$ after the collapse stage. Lin et al.[7] also examined wake characteristics induced by the horizontal motion of a sphere, observing that density stratification suppressed vertical fluid motion. The wake vortex structure evolved into "pancake vortices," with the wavelength (λ) and the Froude number (Fr) of the lee wave satisfying $\lambda/D = 2\pi Fr$.

Bonneton et al.[8] investigated internal gravity waves generated by the horizontal motion of a sphere in a density-stratified flow. They found that the amplitude of the trailing wave decreased as $1/Fr$, while the amplitude of random waves increased with Fr, and wavelength varied as $1/Nt$. Chomaz et al.[9] observed that when $Re > 800$, two unstable modes emerged in the wake under linear density stratification induced by saline solution: the Kelvin–Helmholtz instability and the spiral mode. Spedding[10] proposed that wake flow evolves through three stages within $10 < Fr < 240$ and $5000 < Re < 12\,000$: three-dimensional turbulence stage (3D, $Nt < 2$), non-equilibrium stage (NEQ, $2 < Nt < 50$), and quasi-two-dimensional stage (Q2D, $Nt > 50$). They also found that the turbulent kinetic energy (E) of wake flow scales as $E \sim Nt^{-0.25}$ ($Nt < 50$) and $E \sim Nt^{-0.76}$ ($Nt > 50$). Additionally, Spedding et al.[11] determined that within $1 < Fr < 10$ and $1000 < Re < 10\,000$, the wake width (L_w) scales as $L_w/D \sim (x/D)^{1/3}$, the velocity deficit (U_0/U) as $U_0/U \sim (x/D)^{-2/3}$, and the decay rate of the squared vorticity (ω^2) as $\omega^2 \sim Nt^{-1}$.

Bonnier and Eiff[12] conducted experiments on linearly stratified saltwater and identified four wake evolution stages: near wake, collapse, transition zone, and far wake. During the collapse stage, the velocity deficit at the wake centerline temporarily increases, accompanied by elevated average kinetic energy. After the collapse stage, the decay rates of kinetic energy and vorticity follow $U_0 \sim (x/D)^{-0.38}$, which is significantly slower than $U_0 \sim (x/D)^{-1}$ observed in uniform flow. Xiang et al.[13] identified three stages of wake evolution: the initial stage ($Nt < 2$), the middle stage ($2 < Nt < 10$), and the late stage ($Nt > 10$). In the middle stage, the Kelvin–Helmholtz instability governs turbulence evolution. The wake contracts initially, then expands vertically, with its minimum thickness observed at $Nt = 3 \sim 4$. Wake

vorticity is primarily driven by vertical shear, with horizontal shear contributing minimally.

Advances in computer technology have introduced new methods for studying stratified flow. Chen et al.[14] performed coupled simulations of temperature, salinity, and density stratification by customizing user-defined functions (UDFs) in Fluent. They observed high-temperature, low-salinity vortices in the near-wake region and low-temperature, high-salinity vortices on both sides. Ma et al.[15] established a functional relationship between density and temperature by quantifying the influence of temperature and salinity on density. To simplify calculations, temperature was treated as the primary influencing factor, and density stratification was achieved by prescribing a vertical temperature distribution. Huang et al.[16] proposed a temperature-driven density stratification model using the commercial software STAR-CCM+. Wang et al.[17,18] developed a solver, "TwoLiquidMixingskinFoam," in OpenFOAM, which integrates the volume-of-fluid (VOF) method to capture free surfaces. Nadaf et al.[19] utilized OpenFOAM v2012 to simulate three nonlinear density distributions. Jacobs[20] enhanced the buoyantPimpleFoam solver to simulate propeller rotation in stratified flow.

Numerous researchers have achieved density stratification by defining a functional relationship between temperature and density. When accounting for temperature effects, the dimensionless Prandtl number (Pr) should be considered and is defined as

$$Pr = \frac{\nu}{\alpha}, \tag{6}$$

where ν and α represent molecular viscosity and thermal diffusivity, respectively. The Prandtl number (Pr) quantifies the relative magnitudes of momentum transfer and heat transfer in a fluid. $Pr > 1$ indicates that momentum transfer occurs faster than heat transfer. Using direct numerical simulation (DNS), De Stadler et al.[21] investigated the effects of different Prandtl numbers on wake dynamics. They observed that density disturbances persisted longer at higher Prandtl numbers ($Pr = 7$), while flow mixing efficiency was greater at lower Prandtl numbers ($Pr = 0.2$) compared to higher values ($Pr = 7$). In contrast, the Prandtl number exhibited minimal influence on the wake width, height, and defect velocity.

Other researchers have made significant advances in simulating stratified flow through in-house codes. Diamessis et al.[22] employed the spectral multidomain penalty method to study stratified wake characteristics at high Reynolds numbers and varying internal Froude numbers. Brucker and Sarkar[23] utilized direct numerical simulation (DNS) to compare wakes under drag and self-propelled conditions, observing that turbulence kinetic energy (TKE) decays faster under self-propelled conditions ($Nt < 30$). They also identified a non-equilibrium phase (NEQ) in both drag and self-propelled wakes. Pal et al.[24] used direct numerical simulation (DNS) and the immersed boundary method (IBM) to accurately simulate the surface boundary layer and separation characteristics of a sphere. They found that at lower Fr, turbulent kinetic energy (TKE) gradually shifted from the vertical to the horizontal direction. Redford et al.[25] examined the interactions and dynamic mechanisms among turbulent kinetic energy (TKE), turbulent potential energy (TPE), and mean kinetic energy (MKE). Additionally, most studied wakes were in the near-field region, which could be extended to downstream areas using temporal models and spatiotemporal transformations (e.g., Galilean transformation) to link temporal evolution with spatial position.[26–29]

25 February 2025 14:59:01

Previous numerical simulation studies primarily focused on spheres; however, recent research has shifted attention to other geometries. We conducted parametric studies on the motion of underwater vehicles in the two-layer fluid using large eddy simulation (LES).[30] Ortiz-Tarin *et al.*[31] employed large eddy simulation (LES) to examine the wake of a prolate spheroid with an aspect ratio of 4, showing that the defect velocity scales as $u_d \sim x^{-0.22}$. Ortiz-Tarin *et al.*[32] also employed hybrid simulation for a prolate spheroid with an aspect ratio of 6. They found that wake velocity losses scale as $u_d \sim x^{-2/3}$ (3D), $u_d \sim x^{-0.25}$ (NEQ), and $u_d \sim x^{-0.75}$ (Q2D). Ohh and Spedding[33] examined the wake evolution characteristics of a prolate spheroid with a length-to-diameter ratio of 6 under varying Froude numbers (*Fr*) and angles of attack (θ).

In the numerical simulation of stratified flow, direct numerical simulation (DNS) is predominantly employed,[19,34–37] with spheres being the primary focus of study. While some studies have investigated prolate spheroids, with limited attention to the transition from spherical to prolate spheroidal geometries, the differences in flow mechanisms between spheres and prolate spheroids in stratified flow remain unclear, and this transition introduces changes in curvature and streamlining, which can significantly alter wake mechanisms. The influence of these geometric changes on wake energy dynamics and turbulent kinetic energy (TKE) budgets remains poorly understood. Moreover, the anisotropic geometry of prolate spheroids adds complexity to numerical simulations and flow analysis.[38–40] An increase in aspect ratio significantly enlarges the wake area, necessitating higher grid resolution and smaller time steps. For large eddy simulation (LES) and direct numerical simulation (DNS), the computational cost of simulating prolate spheroids is considerably higher compared to spheres.

This study employs large eddy simulation (LES) and the Boussinesq approximation to investigate the wake variation characteristics in linear stratified flow and addresses these gaps by systematically analyzing the wakes behind prolate spheroids with varying aspect ratios ($L/D = 1.0$ to 3.0). The research primarily focuses on the effects of different aspect ratios on defect velocity, wake length scales, root mean square (RMS) values of velocity components, power spectra, wake energy, and turbulent kinetic energy. The structure of this article is as follows: Sec. II details the methods used for numerical simulations. Section III describes the geometry for different aspect ratios, computational domain setup, and method validation. Section IV presents the numerical simulations of wake flow for different aspect ratios, and Sec. V summarizes and discusses the results.

II. NUMERICAL METHODS
A. Governing equations

This study utilizes the commercial software STAR-CCM+ 2023[41] for numerical simulations. This study employs the large eddy simulation (LES) method to solve spatially filtered control equations under the Boussinesq approximation. Subgrid models are introduced to represent small-scale eddies, including the Smagorinsky model, the dynamic subgrid model, and the wall-adapting local eddy (WALE) model. This study specifically employs the WALE subgrid-scale (SGS) model. The nondimensional governing equations solved in this study are presented as follows:

Mass

$$\frac{\partial u_i}{\partial x_i} = 0. \tag{7}$$

Momentum

$$\frac{\partial u_i}{\partial t} + u_j \frac{\partial u_i}{\partial x_j} = -\frac{\partial p}{\partial x_i} + \frac{1}{Re}\frac{\partial}{\partial x_j}\left[\left(1 + \frac{v_{sgs}}{v}\right)\frac{\partial u_i}{\partial x_j}\right] - \frac{1}{Fr^2}\rho_d\delta_{i3}. \tag{8}$$

Density

$$\frac{\partial \rho}{\partial t} + u_j \frac{\partial \rho}{\partial x_j} = \frac{1}{Re}\frac{\partial}{\partial x_j}\left[\left(1 + \frac{v_{sgs}}{v}\right)\frac{\partial u_i}{\partial x_j}\right], \tag{9}$$

where ρ_d, δ_{i3}, v_{sgs}, v, and p represent, respectively, the deviation in density relative to the background density, the Kronecker delta, the subgrid viscosity, the constant kinematic viscosity, and the filtered pressure.

B. Reynolds decomposition

For clarity in subsequent data analysis, after reaching statistical steady state, each variable is decomposed into a mean component and a fluctuation component through Reynolds decomposition

$$u_i = \overline{u}_i + u_i', \tag{10}$$
$$p = \overline{p} + p', \tag{11}$$
$$\rho = \overline{\rho} + \rho', \tag{12}$$

where $\overline{u}_i$, $\overline{p}$, and $\overline{\rho}$ represent the mean velocity, mean pressure, and mean density, respectively. u_i', p', and ρ' denote the fluctuations of these three variables, respectively. In the following content, variables denoted by a superscript "−" represent mean quantities, while those with a superscript "′" denote fluctuating quantities.

C. Numerical scheme

This study employs the finite volume method for numerical simulation, utilizing a first-order implicit scheme for time discretization. A bounded central scheme is applied for spatial discretization, which combines the accuracy of the central difference scheme with a bounded formulation to prevent numerical oscillations in high-gradient regions. This approach ensures improved resolution of critical flow structures, such as boundary layers and shear layers, while maintaining numerical stability in regions with steep density gradients and complex wake dynamics. The bounded central scheme achieves a balance between accuracy and computational efficiency, making it well-suited for the current LES simulations. The SIMPLE algorithm is used to iteratively solve the pressure–velocity coupling problem. Additionally, the segregated flow approach is adopted to solve the conservation equations for momentum and mass. The non-dimensional time step $\Delta t^* = \Delta t \cdot U/D$ is chosen to be 0.005, where D and U denote the characteristic length and velocity, respectively. This value ensures a Courant number of less than 1, guaranteeing numerical stability.
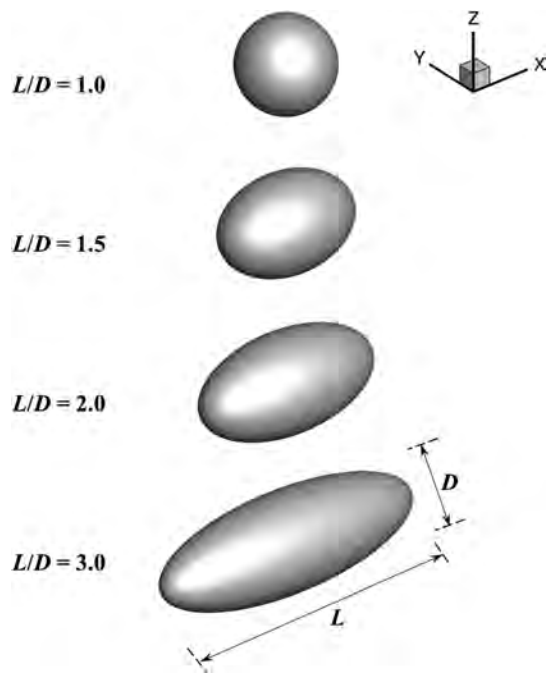
FIG. 1. Geometric model used for simulation.

III. NUMERICAL VALIDATION

A. Geometric model

As shown in Fig. 1, the prolate spheroids used are all bodies of revolution, which are surfaces generated by rotating a generatrix around an axis. D represents the maximum rotation diameter, and L is the maximum length of the body of revolution along the x axis. The aspect ratio, L/D, defines the geometry of each body. Four prolate spheroids are considered in this study, all sharing the same D value, with aspect ratios of 1.0, 1.5, 2.0, and 3.0, respectively. When $L/D = 1.0$, the prolate spheroid is actually a sphere. This design allows us to analyze how changes in curvature and streamlining influence wake structures, velocity deficits, and energy dynamics.

B. Computational domain and boundary condition

The computational domain setup is illustrated in Fig. 2. Given $Fr = 3$, the upstream length of the computational domain is set to $10\,D$
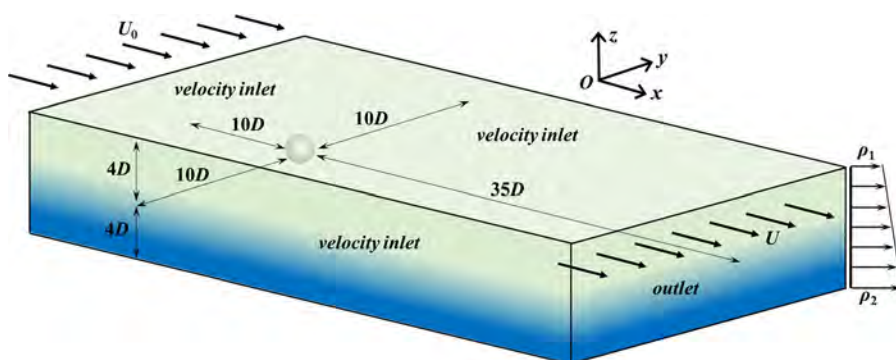
to prevent reflection interference caused by the entrance being too close to the prolate spheroid. The downstream length of the domain extends to $35\,D$. To avoid flow interference from the lateral boundaries, the distances from both sides of the computational domain to the prolate spheroid are $10\,D$. The vertical height of the computational domain is set to $8\,D$.

For the boundary conditions, the upstream boundary of the computational domain is set as velocity inlet, while the downstream boundary is defined as outlet. The lateral sides, as well as the upper and lower boundaries of the computational domain, are also set as velocity inlet. The surface of the prolate spheroid is prescribed as no-slip wall boundary condition, and the density is linearly distributed along the vertical direction.

C. Mesh generation

ICEM CFD is employed to generate a structured mesh for discretizing the entire computational domain, as shown in Fig. 3. The prolate spheroid is positioned at the center of the computational domain, with mesh refinement applied near its surface to capture the flow characteristics of the boundary layer and near-wall region. Radial mesh refinement is also performed along the surface, while additional refinement is applied in the core region of wake development to enhance resolution. The mesh size gradually increases in regions farther from the prolate spheroid. The entire computational domain consists of approximately 15 million cells.

D. Model validation and verification

To further evaluate the quality of grid, the ratio of the grid size at various positions in the x, y, and z directions to the Kolmogorov length scale (η) is calculated, which represents the smallest dissipative turbulent structures, as shown in Fig. 4. This approach is widely used in LES studies, as the Kolmogorov scale is directly linked to the energy dissipation range, making it a more relevant metric for assessing grid adequacy in LES compared to the Taylor scale. The Kolmogorov length scale is defined as $\eta = (\nu^3/\varepsilon)^{1/4}$, where ν is the kinematic viscosity and ε is the turbulent dissipation rate, which is calculated under unstratified flow. In Figs. 4(a) and 4(c), the values of $\Delta x/\eta$ and $\Delta z/\eta$ are less than 20. In Fig. 4(b), at $x/D = 2.5$ and $z/D = 0$, the worst value of $\Delta y/\eta$ is approximately 20. When Chongsiripinyo and Sarkar[28] conducted numerical simulations based on LES ($Re = 5 \times 10^4$, $Fr = 2, 10, 50, \infty$), the worst grid quality is $\Delta x/\eta = 17$. In comparison, in this study, the $\Delta x/\eta$ value is relatively similar when the Froude number is comparable and the Reynolds number is an order of magnitude smaller than in
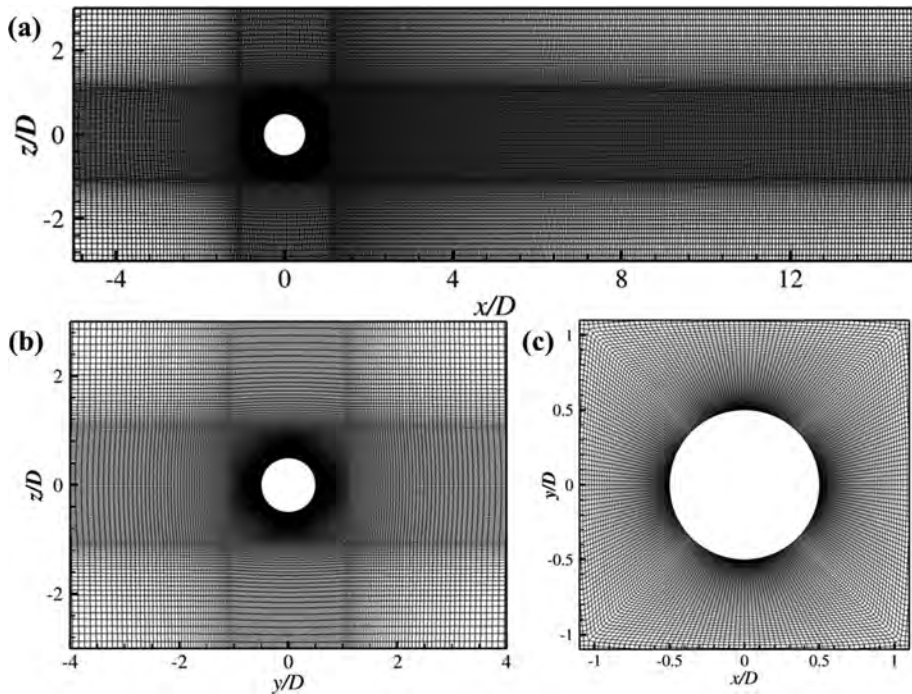

FIG. 2. Computational domain setup.

FIG. 3. Computational mesh (enlarged view). (a) x-z cross section; (b) y-z cross section, and (c) x-y cross section.

their study, indicating that the overall grid quality in this work is of high resolution.

After assessing the quality of grid, the validation of numerical simulation methods is performed. The validation process is divided into two parts. First, method validation under unstratified flow is

conducted, as shown in Fig. 5. Numerical simulations under unstratified flow are carried out, and Figs. 5(a) and 5(b) illustrate the pressure coefficient (C_p) and shear stress coefficient ($(\tau/\rho U^2 Re^{0.5})$, τ is the shear stress) on the prolate spheroid surface as functions of the azimuthal angle (θ). The pressure coefficient agrees well with the
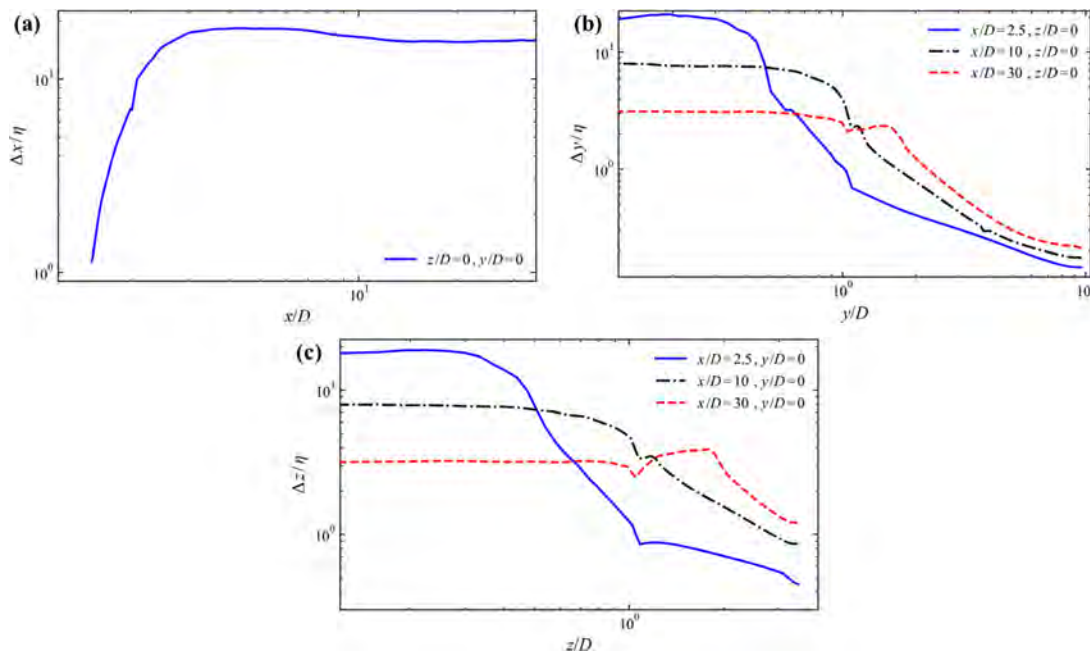

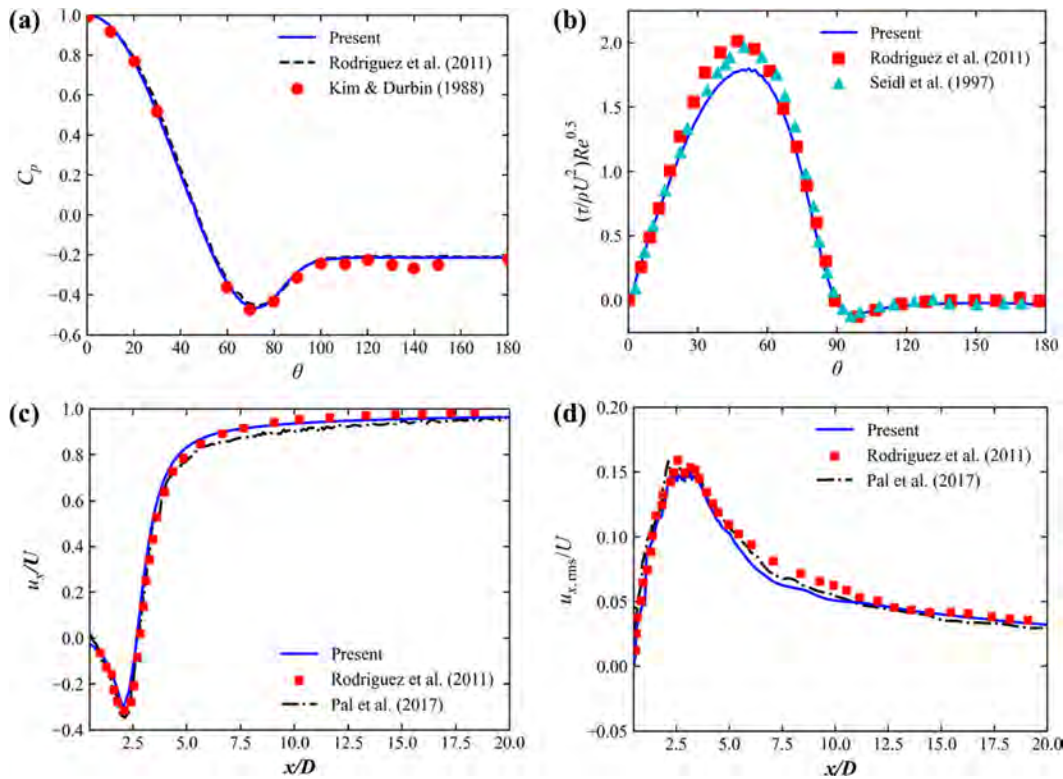**FIG. 4.** Grid quality. (a) streamwise size; (b) lateral size, and (c) vertical size.

FIG. 5. Validation of the unstratified flow: (a) the pressure coefficient; (b) the shear stress coefficient; (c) streamwise velocity; and (d) r.m.s. streamwise velocity.

experimental results of Kim and Durbin[5] and the DNS results of Rodriguez et al.[42] Similarly, the shear stress coefficient aligns well with the DNS results of Rodriguez et al.[42] and Seidl et al.[43] Figs. 5(c) and Fig. 5 present streamwise velocity (u_x) and the root mean square value of the streamwise velocity ($u_{x,rms}$) at the wake centerline. These results show good agreement with the DNS results of Pal et al.[44] and Rodriguez et al.[42]

The method is subsequently validated under stratified flow. Figures 6(a) and 6(b) depict the defect velocity (u/U) at the wake centerline and the root mean square (RMS) values of the streamwise

velocity ($u_{x,rms}/U$). Bonnier and Eiff[12] conducted experiments at $Fr = 3$ and $Re = 6900$, featuring higher Reynolds numbers compared to the studies by Nadaf et al.[19] ($Re = 3700$, $Fr = 3$) and Pal et al.[44] ($Re = 3700$, $Fr = 3$). For defect velocity, the results match well with the DNS of Pal et al.[44] Regarding the RMS values of streamwise velocity, the results show good agreement with the DNS of Pal et al.[44] and the experimental results of Bonnier and Eiff.[12]

The adequacy of the grid resolution is further validated through benchmarking against published results for both unstratified and stratified flows. The close agreement with prior studies confirms that the
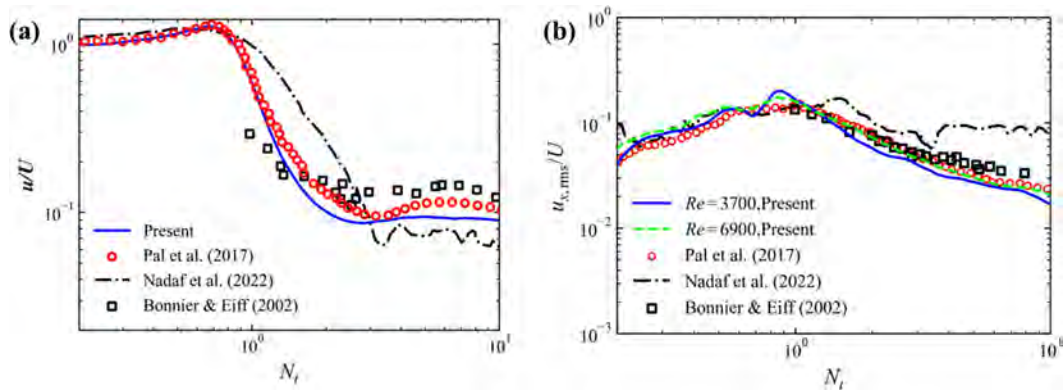

FIG. 6. Validation of the stratified flow: (a) velocity deficit and (b) r.m.s. streamwise velocity.

25 February 2025 14:59:01

TABLE I. Computational conditions.

Case	L/D	Re	Fr	Pr
1	1.0	3700	3	1
2	1.5	3700	3	1
3	2.0	3700	3	1
4	3.0	3700	3	1

grid sufficiently captures the key wake dynamics and turbulence characteristics under the studied conditions.

IV. RESULTS AND DISCUSSION

Table I presents the simulation parameters, primarily focusing on comparisons of aspect ratios. All simulations are conducted at $Re = 3700$, $Fr = 3$, and $Pr = 1$. The values $Re = 3700$ and $Fr = 3$ are chosen to facilitate method validation, as discussed earlier, and to enable comparisons with the studies of Pal et al.,[44] Rodriguez et al.,[42] Seidl et al.,[43] and Nadaf et al.[19] The selection of $Pr = 1$ follows the recommendations from Stadler et al.[21] At $Pr = 1$, the rates of momentum diffusion and heat diffusion are equal, which avoids complex linear coupling effects, simplifies calculations, and improves the convergence and stability of the simulations.

A. Visualization of wake

Figure 7 illustrates the vorticity distribution of the wake for different aspect ratios. As the aspect ratio increases, the vertical extent of the wake decreases, and the intensity of vorticity diminishes correspondingly. When the aspect ratio is small ($L/D = 1.0$ and $L/D = 1.5$), the close proximity of the front and back ends of the prolate spheroid causes superimposed interference between the front and back flows, leading to more pronounced vortex shedding. Conversely, when $L/D = 3.0$, the increased distance between the front and back ends reduces mutual interaction, the flow of the wake becomes smoother.

The wake vortex structures under different aspect ratios are identified using the Q-criterion method, as illustrated in Figs. 8 and 9. Observations of the vortex structures on the x-y and x-z planes reveal that the distribution range in the vertical direction is significantly smaller than in the horizontal direction under the same aspect ratio, indicating that density stratification suppresses vertical vortex development. At smaller aspect ratios, the distribution range of vortex structures in both the horizontal and vertical directions is larger, and the downstream propagation distance is greater. As the aspect ratio increases, the wake flow stabilizes, and the distribution range of wake vortex structures in all directions decreases significantly.

When comparing different aspect ratios, notable differences arise. For example, at $L/D = 3.0$, there are no flow data within the prolate spheroid in the region $0.5 < x/D < 1.5$. Conversely, at $L/D = 1.0$, wake flow data exist outside the prolate spheroid in the same region. To facilitate meaningful comparisons, the trailing edge of each prolate spheroid is set as its coordinate origin in the subsequent curve analysis. This ensures that wake characteristics specific to each aspect ratio are accurately captured and analyzed.

Figure 10 compares the defect velocity along the centerline of the wake for different aspect ratios. Initially, a recirculation zone is formed,
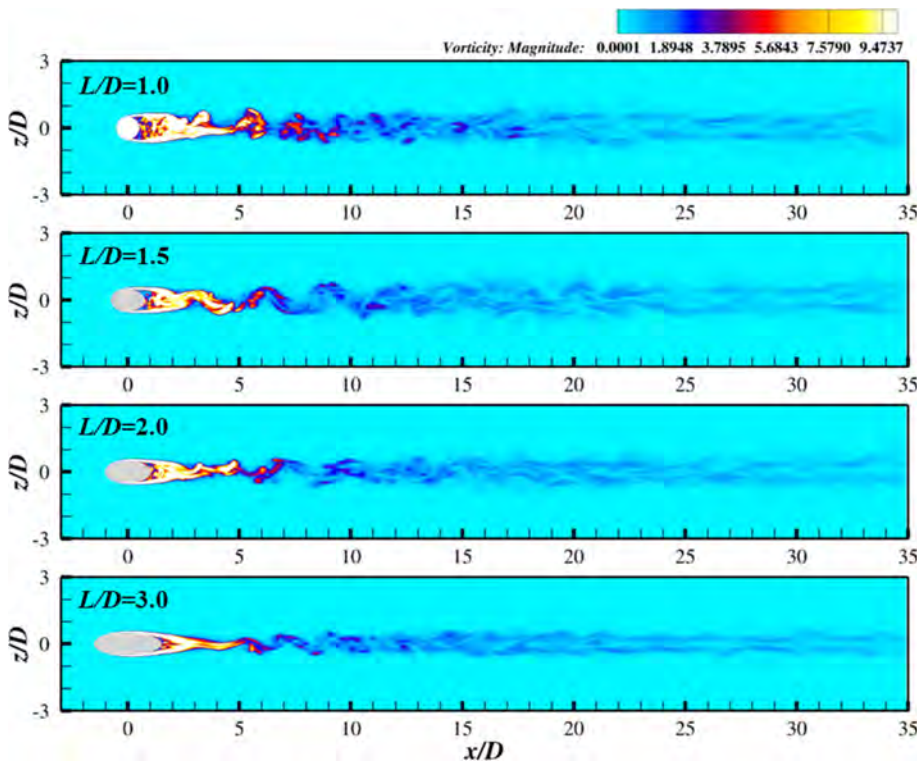

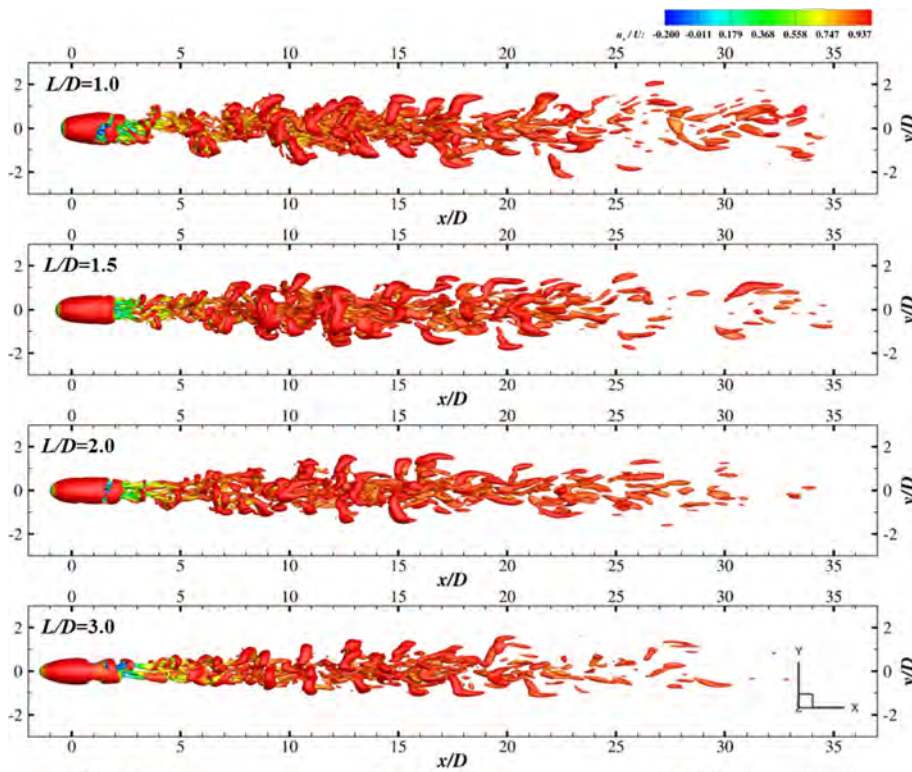**FIG. 7.** Distribution of vorticity at the vertical center plane.

FIG. 8. Vortex structures under different aspect ratios ($Q = 0.1$) (x-y plane).

where the normalized defect velocity exceeds 1. As the aspect ratio increases, the length of the recirculation zone decreases sequentially, measuring 1.92, 1.47, 1.08, and 0.88, respectively. Beyond the recirculation zone, the defect velocity monotonically decreases to a local minimum. The position of this local minimum shifts upstream with increasing aspect ratio. For $L/D = 3.0$, the local minimum occurs at $x/D = 6.4$, This location also occurs earlier than the one observed by Pal et al.[44] The region between the recirculation zone and the local minimum is referred to as the three-dimensional turbulent zone,[10] or the near wake,[12] where buoyancy effects are negligible. Beyond the
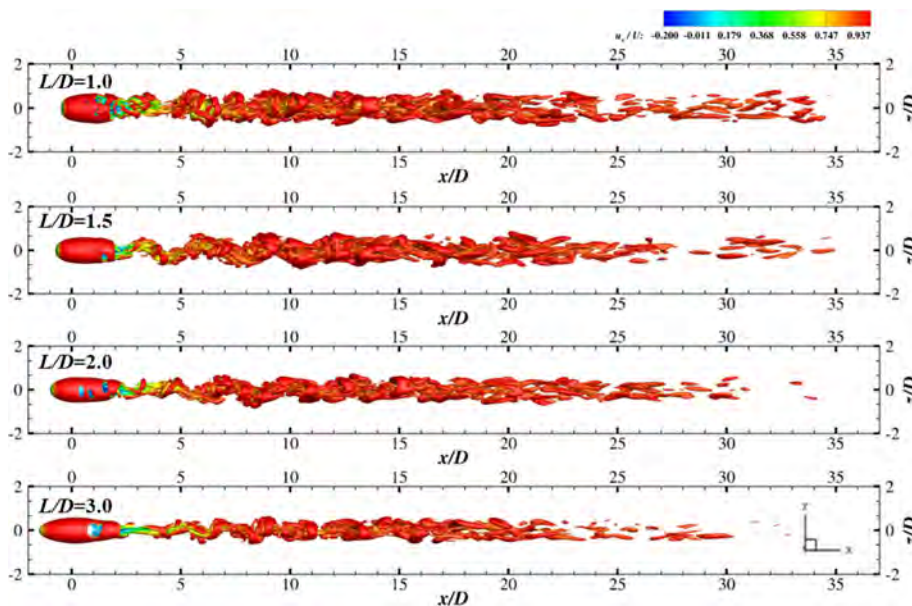

FIG. 9. Vortex structures under different aspect ratios ($Q = 0.1$) (x-z plane).
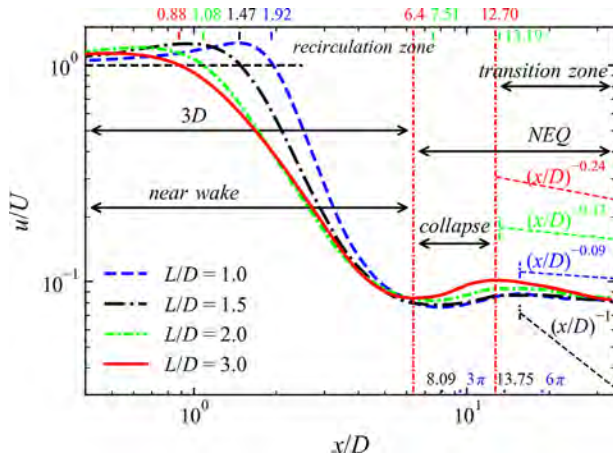
FIG. 10. Defect velocity at the wake centerline for different aspect ratios.

local minimum, the wake enters the non-equilibrium region,[10] where buoyancy begins to suppress vertical wake motion.

In contrast to unstratified flow, where the defect velocity curve monotonically decreases ($u \sim (x/D)^{-1}$) after the recirculation zone, stratified flow exhibits an accelerated collapse stage,[12] also known as oscillatory modulation.[44] During this stage, the defect velocity temporarily increases, reaching a local peak. As the aspect ratio increases, the

position of this peak shifts upstream. Following the accelerated collapse stage, the defect velocity decreases monotonically, marking the transition zone.[12] In the transition zone, the defect velocity for different aspect ratios follows distinct decay rates: $u \sim (x/D)^{-0.08}$ ($L/D = 1.0$), $u \sim (x/D)^{-0.09}$ ($L/D = 1.5$), $u \sim (x/D)^{-0.13}$ ($L/D = 2.0$), and $u \sim (x/D)^{-0.24}$ ($L/D = 3.0$). These rates differ from the $u \sim (x/D)^{-0.25}$ observed by Pal et al.[44] for $L/D = 1.0$ (sphere). As the aspect ratio increases, the defect velocity decays more rapidly, indicating a shorter mean lifespan of the wake. According to existing relationships, for $L/D = n$, the defect velocity satisfies $u \sim (x/D)^{(-0.0327n^2 + 0.0498n - 0.0955)}$.

The half-width of the wake is defined as the distance from the centerline to the position where the defect velocity decreases to half its value on the centerline. This definition also applies to the half-height of the wake. In Fig. 11(a), the half width of the wake (L_H) decreases gradually within the recirculation zone and reaches a local minimum near the end of recirculation zone. In Fig. 11(b), the half-height of the wake (L_V) reaches a local minimum at approximately $x/D = 1.92$ and a peak near $x/D = 6.4$. A comparison of Figs. 11(a) and 11(b) indicates that the aspect ratio primarily influences the location of the local minimum of the wake half-width. In Fig. 11(c), the ratio of the wake half height to half width is less than 1, indicating significant anisotropy in the wake vertical and horizontal dimensions. From Figs. 11(a)–11(d), it is evident that as the aspect ratio increases, the half-width, half-height, the ratio of half-height to half-width, and the area of wake all decrease. These quantities reach maximum values near the onset of the accelerated collapse stage. Subsequently, periodic oscillations occur
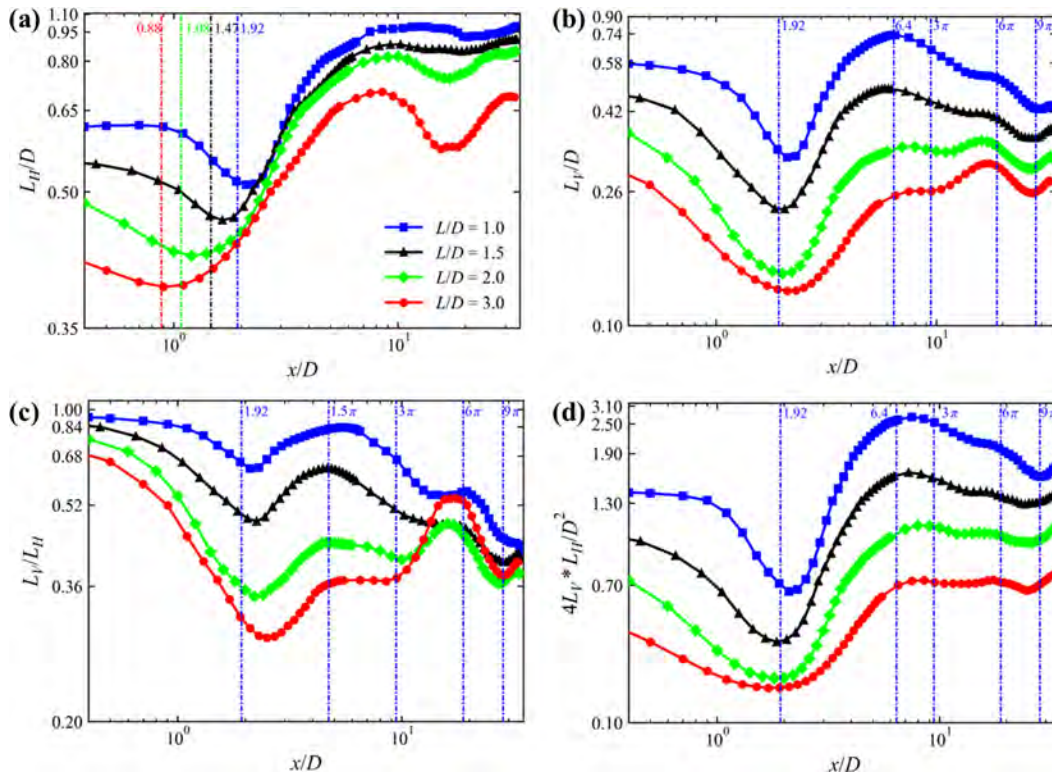

FIG. 11. The thickness of the wake for different aspect ratios. (a) half-widths in the horizontal direction; (b) half-widths in the vertical direction; (c) aspect ratio of vertical wake span to horizontal wake span; and (d) the area of the wake region (roughly).

within the range $\pi Fr < x/D < 3\pi Fr$. The peak values are observed at one buoyancy period ($Nt = 2\pi$), and the valley values appear at 1.5 buoyancy periods ($Nt = 3\pi$).

B. Turbulence levels

Figure 12 shows the root mean square (RMS) values of the streamwise velocity, spanwise velocity, vertical velocity, and density deviation. The RMS values of the velocity components are normalized by the flow velocity U. The density deviation is normalized using the density difference between the upper and lower boundaries of the computational domain.

The overall trend observed for the four quantities is that the root mean square (RMS) values decrease as the aspect ratio increases. At the same aspect ratio, comparing the RMS values of the three velocity components reveals that the vertical velocity has smaller RMS values compared to the streamwise and spanwise velocities. This indicates that at $Fr = 3$, vertical motion in the wake is suppressed, streamwise velocity dominates, and the wake velocity exhibits pronounced anisotropy across all directions. Additionally, in Figs. 12(a) and 12(b), the streamwise and spanwise velocities decrease approximately monotonically beyond $x/D = 1.92$. In contrast, the vertical velocity and density oscillate periodically, suggesting that the two quantities are significantly influenced by buoyancy.

For vertical velocity, the root mean square (RMS) value reaches a local minimum near the beginning of the accelerated collapse stage

and subsequently attains local peaks at different positions ($x/D = 12.70, 22.12$, and 31.55). The spacing between these positions corresponds to half a buoyancy period (πFr). For density, a local minimum is observed at positions corresponding to the vertical velocity peaks, with the spacing between these locations also satisfying half a buoyancy period. This indicates that the wake undergoes periodic oscillations driven by buoyancy and inertial forces, leading to periodic oscillations in both vertical velocity and density.

The expression for Reynolds stress is as follows:

$$\tau_{ij} = -\rho \overline{u_i' u_j'}. \tag{13}$$

Reynolds stress is nondimensionalized by normalizing with $\rho_0 U^2$, where ρ_0 is the initial density at the centerline of the prolate spheroid, and U is the velocity of the incoming flow. Figure 13 illustrates the distributions of $\tau_{xx}, \tau_{xz}, \tau_{zz}$, and τ_{xy}. The regions of increased Reynolds stress are observed to lie within the recirculation zone.[45] For smaller aspect ratios, the vertical distribution range of Reynolds stress is broader, and the magnitudes are higher. Conversely, as the aspect ratio increases, Reynolds stress becomes concentrated near the centerline, and magnitude decreases significantly.

C. Spectra

Four sampling points are set in the computational domain at dimensionless positions $(2.0,0,0.51)$, $(6.5,0,0.51)$, $(13.0,0,0.51)$, and $(30,0,0.51)$. The first point is located at the end of the recirculation
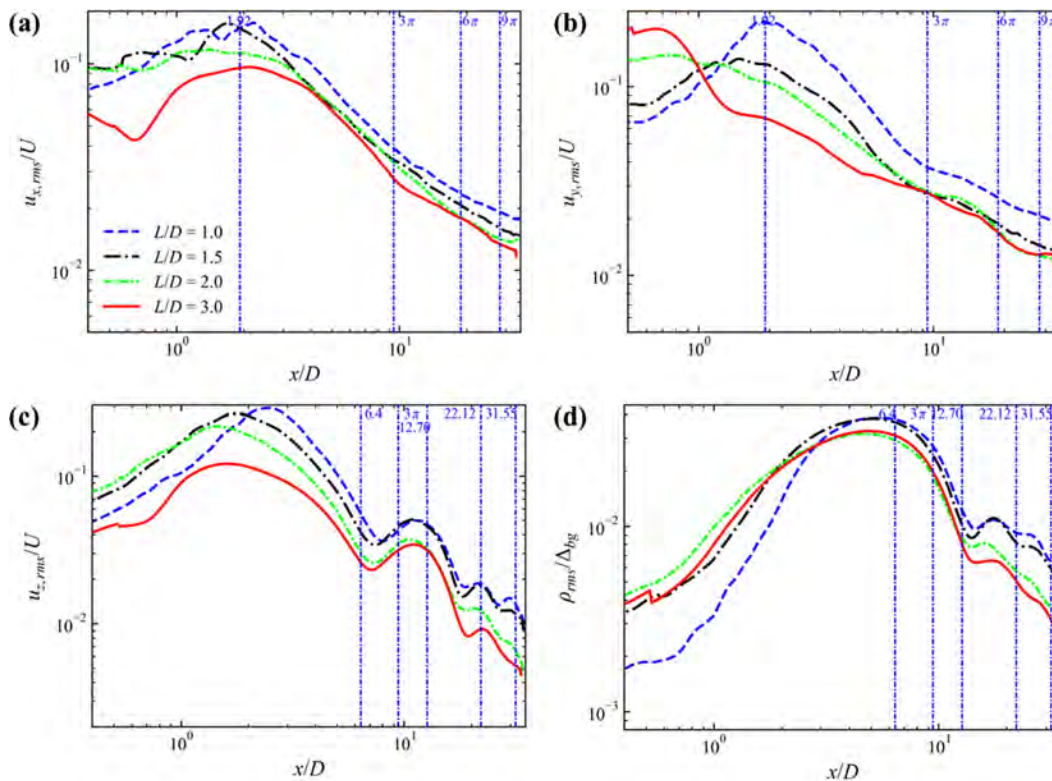

FIG. 12. Root mean square value of variables for different aspect ratios. (a) streamwise velocity; (b) lateral velocity; (c) vertical velocity; and (d) the change in density.
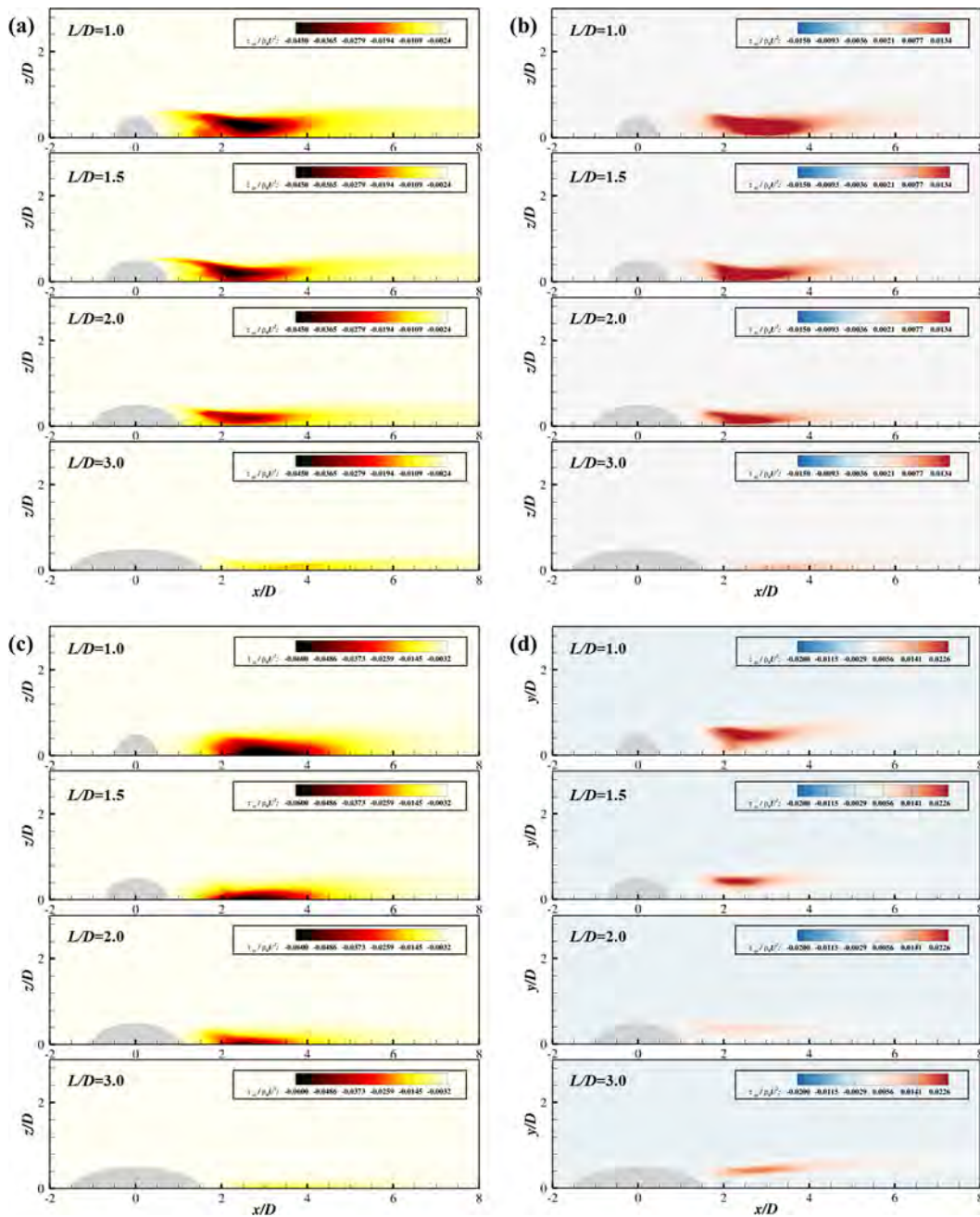
FIG. 13. Normalized average Reynolds stress for different aspect ratios. (a) τ_{xx}; (b) τ_{xz}; (c) τ_{zz}; and (d) τ_{xy}.

zone, the second at the beginning of the accelerated collapse stage, the third at the position where a local peak is reached after the accelerated collapse, and the fourth in a region farther from the wake. Sampling begins after the incoming stream has flowed through the entire computational domain for three cycles and ends after nine cycles, with a sampling interval of 0.002 s.

Figure 14 presents the power spectra of the streamwise velocity at the four sampling points. As the aspect ratio increases, the energy across different frequencies (f) gradually decreases. At the first point, the energy difference among the four aspect ratios is the largest, and this difference diminishes progressively at farther positions. At the first sampling point, the inertial subrange satisfying the $-5/3$ slope lies between $1 < f < 5$. As the distance increases, the extent of the inertial subrange satisfying the $-5/3$ slope decreases.

Power spectra of the vertical velocity at the four sampling points are shown in Fig. 15. The pattern resembles that of the streamwise

25 February 2025 14:59:01
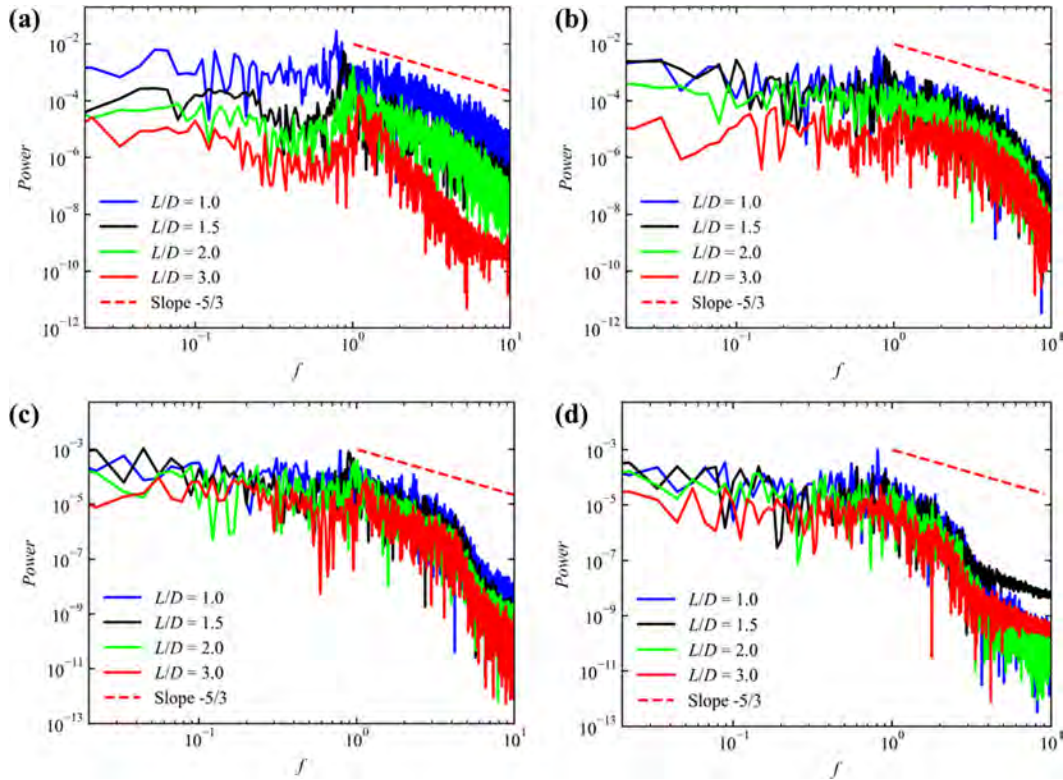
FIG. 14. Power spectra of the streamwise velocity for different aspect ratios. (a) at $x/D = 2.0$, $y/D = 0$, $z/D = 0.51$; (b) at $x/D = 6.5$, $y/D = 0$, $z/D = 0.51$; (c) at $x/D = 13.0$, $y/D = 0$, $z/D = 0.51$; and (d) at $x/D = 30.0$, $y/D = 0$, $z/D = 0.51$.

velocity power spectrum; however, the energy levels of the vertical velocity are significantly lower than those of the flow velocity. Similar to Fig. 14, the power spectrum of the vertical velocity exhibits distinct discrete spectral peaks. As the aspect ratio increases, the frequency values corresponding to these discrete spectral peaks gradually rise. The Strouhal number (St), a dimensionless quantity related to frequency, is calculated based on the discrete spectral peaks for different aspect ratios, yielding $St = 0.26$, 0.28, 0.31, and 0.35. As the aspect ratio increases, the frequency of vortex shedding shows a slight increase. In stratified flow, the narrowing of the wake shear layer contributes to a higher vortex shedding frequency compared to unstratified flow.[46]

D. Energy of wake

In stratified flow, the wake involves not only changes in kinetic energy but also changes in potential energy induced by density stratification. Turbulent potential energy is a unique feature of stratified flow. As noted by Stadler et al.,[44] the total energy (E) of the wake can be decomposed into three components: mean kinetic energy (mke), turbulent kinetic energy (K), and turbulent potential energy ($K\rho$). The expression is given as

$$E = mke + K + K_\rho = \frac{1}{2}\overline{u_i u_i} + \frac{1}{2}\overline{u_i' u_i'} + \frac{1}{2Fr^2}\overline{\rho'\rho'}. \quad (14)$$

The expression for turbulent potential energy is derived from the research of Itswire et al.,[47] incorporating the Froude number (Fr) to

quantify the influence of stratification intensity on turbulent potential energy. At different positions in the wake region, the energy is integrated, with A representing the integrated area. The formulas for area integral are defined as follows:

$$MKE = \int_A mke \, dA, \quad (15)$$

$$TKE = \int_A K \, dA, \quad (16)$$

$$TPE = \int_A K_\rho \, dA. \quad (17)$$

Figure 16 shows that the total energy, turbulent kinetic energy, mean kinetic energy, and turbulent potential energy of the wake all decrease as the aspect ratio increases. Among the different energy components, mean kinetic energy dominates the energy distribution within the wake. The total energy and turbulent potential energy reach maximum values near the beginning of the accelerated collapse stage ($x/D = 6.4$). Near the end of the accelerated collapse stage ($x/D = 12.70$), where defect velocity occurs a local peak, the total energy, turbulent potential energy, and turbulent kinetic energy begin periodic oscillations. The oscillation period corresponds to half a buoyancy period (πFr). A key difference is observed: the total energy and turbulent potential energy exhibit local troughs at $x/D = 12.70$, 22.12, and 31.55, while turbulent kinetic energy shows local peaks at these positions.
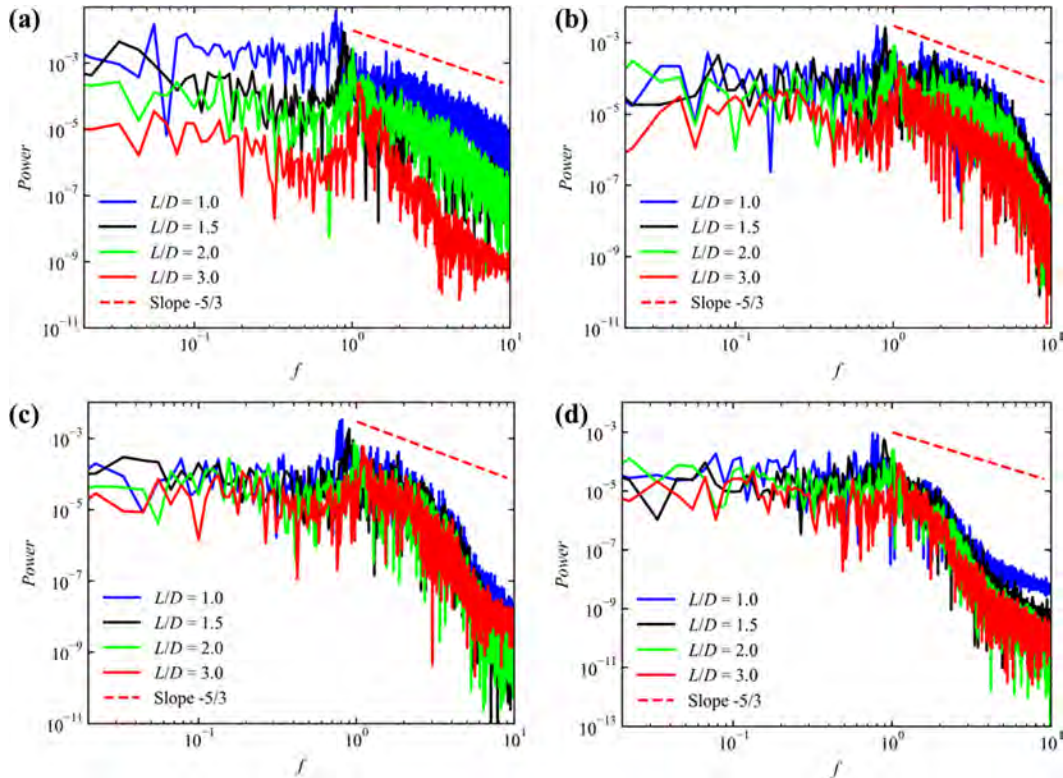
FIG. 15. Power spectra of the vertical velocity for different aspect ratios. (a) at $x/D = 2.0$, $y/D = 0$, $z/D = 0.51$; (b) at $x/D = 6.5$, $y/D = 0$, $z/D = 0.51$; (c) at $x/D = 13.0$, $y/D = 0$, $z/D = 0.51$; and (d) at $x/D = 30.0$, $y/D = 0$, $z/D = 0.51$.

The maximum turbulent kinetic energy occurs near the end of the recirculation zone. Additionally, turbulent kinetic energy at different aspect ratios follows the relationship TKE $\sim (x/D)^{-1.19}$.

In the turbulent kinetic energy of the wake, the buoyancy flux term is used to quantify the energy transfer between turbulent kinetic energy and turbulent potential energy. The expression for the buoyancy flux term is provided in Eq. (18). The expression for the turbulent dissipation term in the turbulent kinetic energy of the wake is shown in Eq. (19)

$$B = -\frac{1}{Fr^2} \overline{\rho' u'_3}, \tag{18}$$

$$\varepsilon = -\frac{1}{Re} \overline{\left(1 + \frac{v_{sgs}}{v}\right) \frac{\partial u'_i}{\partial x_i} \frac{\partial u'_i}{\partial x_i}}. \tag{19}$$

The mixing efficiency of the wake quantifies the energy utilization efficiency during the fluid mixing process, and its traditional expression is provided in Eq. (20). The traditional expression for the mixing efficiency of the wake is not suitable for stratified flow, as the buoyancy flux term oscillates between negative and positive values, leading to both positive and negative overall efficiency values.[44] Furthermore, when the magnitude of the buoyancy flux term equals that of the turbulent dissipation term, opposing signs can result in mutual cancelation. This cancelation may produce anomalous values for the mixing efficiency, such as negative values or unrealistically maxima, which do

not align with the actual physical meaning of mixing efficiency in stratified flow. Stadler *et al.*[44] introduced a scalar dissipation term, expressed in Eq. (21). While turbulent kinetic energy is primarily dissipated through the turbulent dissipation rate, turbulent potential energy is predominantly dissipated through the scalar dissipation term. This term essentially represents the degree to which density stratification is disrupted. By incorporating the scalar dissipation term, the wake mixing efficiency in density-stratified flows has been redefined, as shown in Eq. (22)

$$\eta = \frac{\int_A B \, dA}{\int_A B \, dA + \int_A \varepsilon \, dA}, \tag{20}$$

$$\varepsilon_\rho = -\frac{1}{Pr \, Re \, Fr^2} \overline{\left(1 + \frac{v_{sgs}}{v}\right) \frac{\partial \rho'}{\partial x_i} \frac{\partial \rho'}{\partial x_i}}, \tag{21}$$

$$\eta = \frac{\int_A \varepsilon_\rho \, dA}{\int_A \varepsilon_\rho \, dA + \int_A \varepsilon \, dA}. \tag{22}$$

Figure 17 compares the distributions of turbulent kinetic energy (TKE) and turbulent potential energy (TPE) in the wake region at the same aspect ratio and presents the corresponding wake mixing
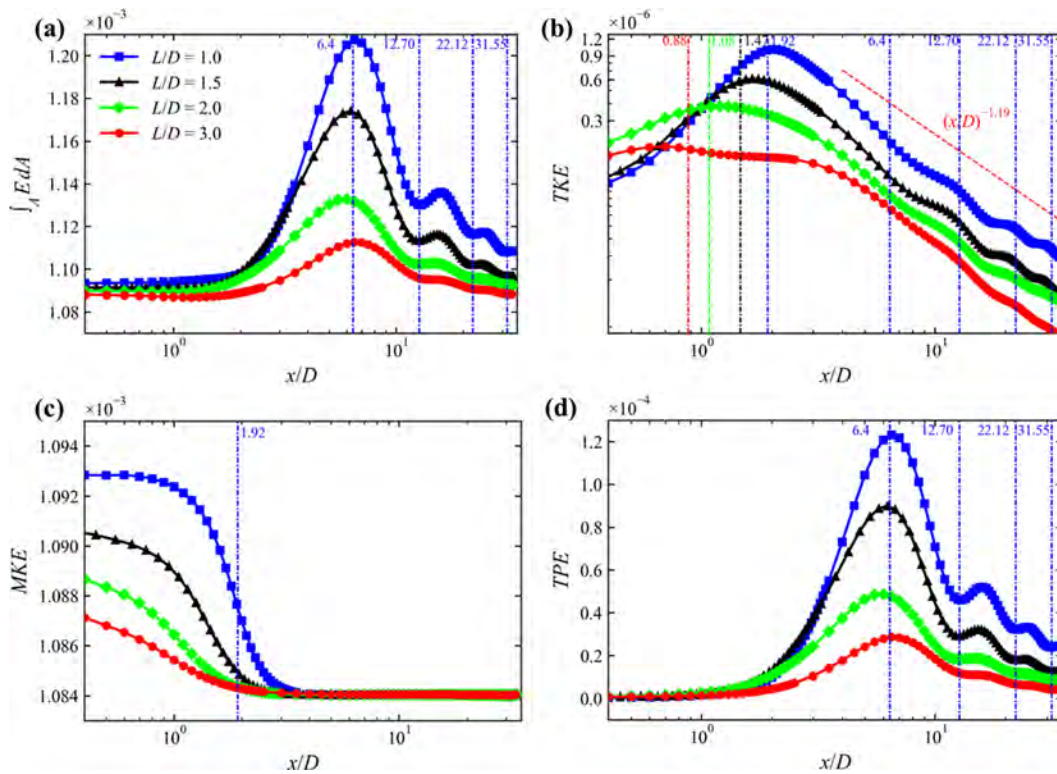
FIG. 16. Area integrated energy for different aspect ratios. (a) total energy; (b) turbulent kinetic energy; (c) mean kinetic energy; and (d) turbulent potential energy.

efficiency (η). The peak positions of TKE and TPE do not coincide. As previously analyzed, the peak position of TKE is located within the recirculation zone, where turbulence intensity is relatively high, and the turbulent dissipation rate dominates. At this stage, the mixing efficiency of the wake is relatively low. As the wake progresses downstream, turbulence intensity weakens, TPE gradually increases, and the scalar dissipation term begins to dominate. This shift results in an increase in wake mixing efficiency. Near the beginning of the accelerated collapse stage, as discussed earlier, TPE reaches peak, and the corresponding wake mixing efficiency also reaches maximum value. Beyond this position, the wake mixing efficiency curve stabilizes, approaching a value of 1.

Figure 18 illustrates the variations in wake mixing efficiency under different aspect ratios. The mixing efficiency reaches minimum value within the recirculation zone and peaks near the beginning of the accelerated collapse stage. Beyond this position, the mixing efficiency stabilizes as the aspect ratio increases. Before the peak mixing efficiency is reached, the efficiency gradually increases with the aspect ratio. This trend reveals that as the aspect ratio increases, the contribution of the scalar dissipation term to the energy dissipation in the wake becomes more significant.

E. Terms in the turbulent kinetic energy budget

The turbulent kinetic energy (K) equation describes the change of energy in turbulence. The form is provided in Eq. (23), where A, P, and T represent the advection term, production term, and transport

term, respectively. The expressions for these three terms are presented in Eqs. (24)–(26). The formulas for the dissipation and buoyancy terms are introduced earlier

$$\frac{\partial K}{\partial t} = A + P + \varepsilon + T + B, \tag{23}$$

$$A = -\overline{u_j}\frac{\partial K}{\partial x_j}, \tag{24}$$

$$P = -\overline{u'_i u'_j}\frac{\partial \overline{u_i}}{\partial x_j}, \tag{25}$$

$$T = -\frac{1}{2}\frac{\partial}{\partial x_i}\overline{u'_i u'_j u'_j} - \frac{\partial}{\partial x_i}\overline{p' u'_i}$$
$$+ \frac{1}{2Re}\frac{\partial}{\partial x_j}\left(\left(1 + \frac{v_{sgs}}{v}\right)\frac{\partial}{\partial x_j}\overline{u'_i u'_i}\right)$$
$$+ \frac{1}{Re}\overline{u'_i\frac{\partial u'_j}{\partial x_i}\frac{\partial(v_{sgs}/v)}{\partial x_j}}. \tag{26}$$

Figure 19 illustrates the distribution of turbulent kinetic energy at various positions in the wake region under different aspect ratios. As the distance from the wake region increases, the values of turbulent kinetic energy gradually decrease. For a sphere with $L/D = 1.0$, at $x/D = 2.0$, the intensity of turbulence is relatively high, and the distribution of turbulent kinetic energy is approximately circular, indicating isotropy in all directions. As the distance increases, buoyancy
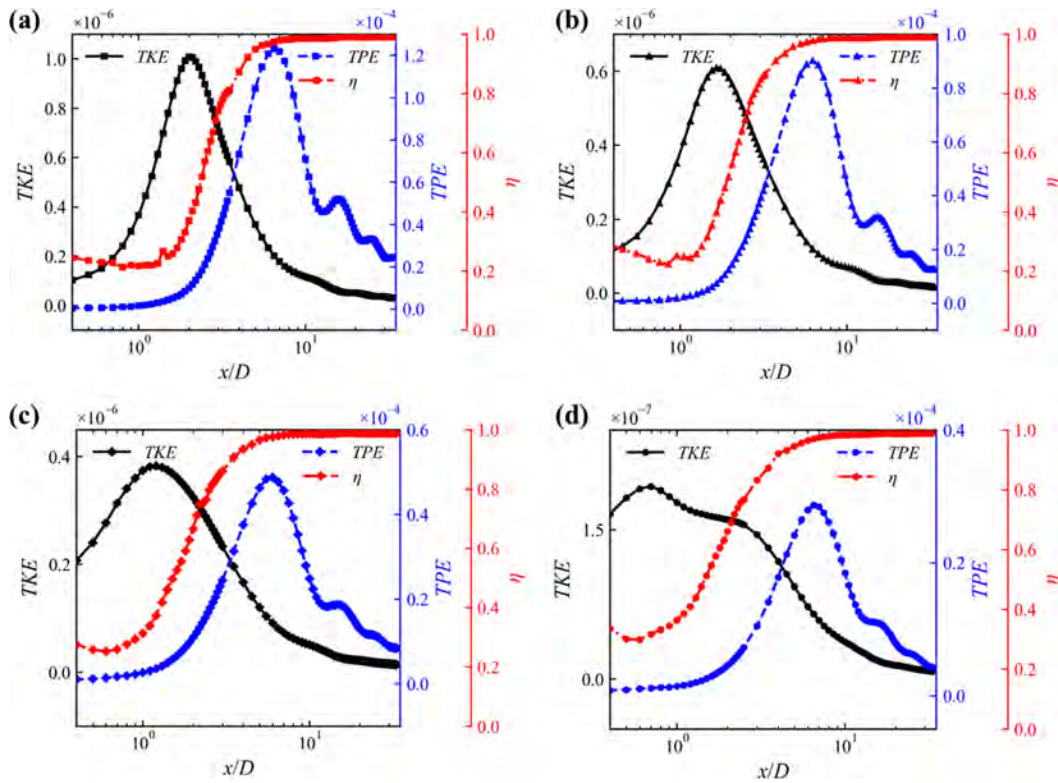
FIG. 17. Mixing efficiency and relative changes in turbulent kinetic energy and turbulent potential energy for different aspect ratios. (a) $L/D = 1.0$; (b) $L/D = 1.5$; (c) $L/D = 2.0$; and (d) $L/D = 3.0$.

suppresses the vertical motion of the wake, and the turbulent energy distribution evolves into an elliptical shape, becoming compressed in the vertical direction and extended horizontally. For higher aspect ratios, such as $L/D = 3.0$, the distribution of turbulent kinetic energy at $x/D = 2.0$ already shows a distinct horizontal elongation. Comparing turbulent kinetic energy at the same position across different aspect ratios reveals that the anisotropy of turbulent kinetic energy becomes

FIG. 18. Mixing efficiency for different aspect ratios.

increasingly pronounced, with the horizontal distribution range exceeding the vertical range.

Figures 20–23 present area integrated of various terms in the turbulent kinetic energy (K) equation across two regions of the wake. The entire wake is divided into two parts: the first region, $0.4 < x/D < 10$, and the second region, $10 < x/D < 35$. Due to the varying magnitudes of the terms, to better observe the changes in each term, Figures (c) and (d) provide enlarged views of Figures (a) and (b), respectively.

In the range $0.4 < x/D < 10$, the peak of the production occurs near the end of the recirculation zone. Beyond this position, production gradually decreases, approaching zero near the beginning of the accelerated collapse stage. Correspondingly, buoyancy reaches a local minimum at this position, coinciding with the location where turbulent kinetic energy reaches maximum. This indicates that negative buoyancy flux converts turbulent kinetic energy into turbulent potential energy.

In the range $10 < x/D < 35$, production becomes negligible, as magnitude is near zero. Dissipation monotonically decreases throughout this region. In contrast, transport, advection, and buoyancy exhibit periodic oscillations, with buoyancy displaying the most prominent periodic variations, the periodic oscillation of the buoyancy term, alternating between positive and negative values, further validates the earlier discussion on the wake mixing efficiency formula. The positions of the peak and valley values align closely with the patterns discussed previously, confirming that the wavelength of the periodic oscillations corresponds to half a buoyancy period (πFr).
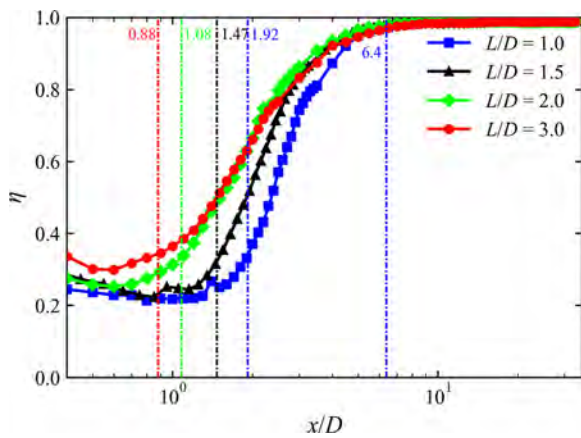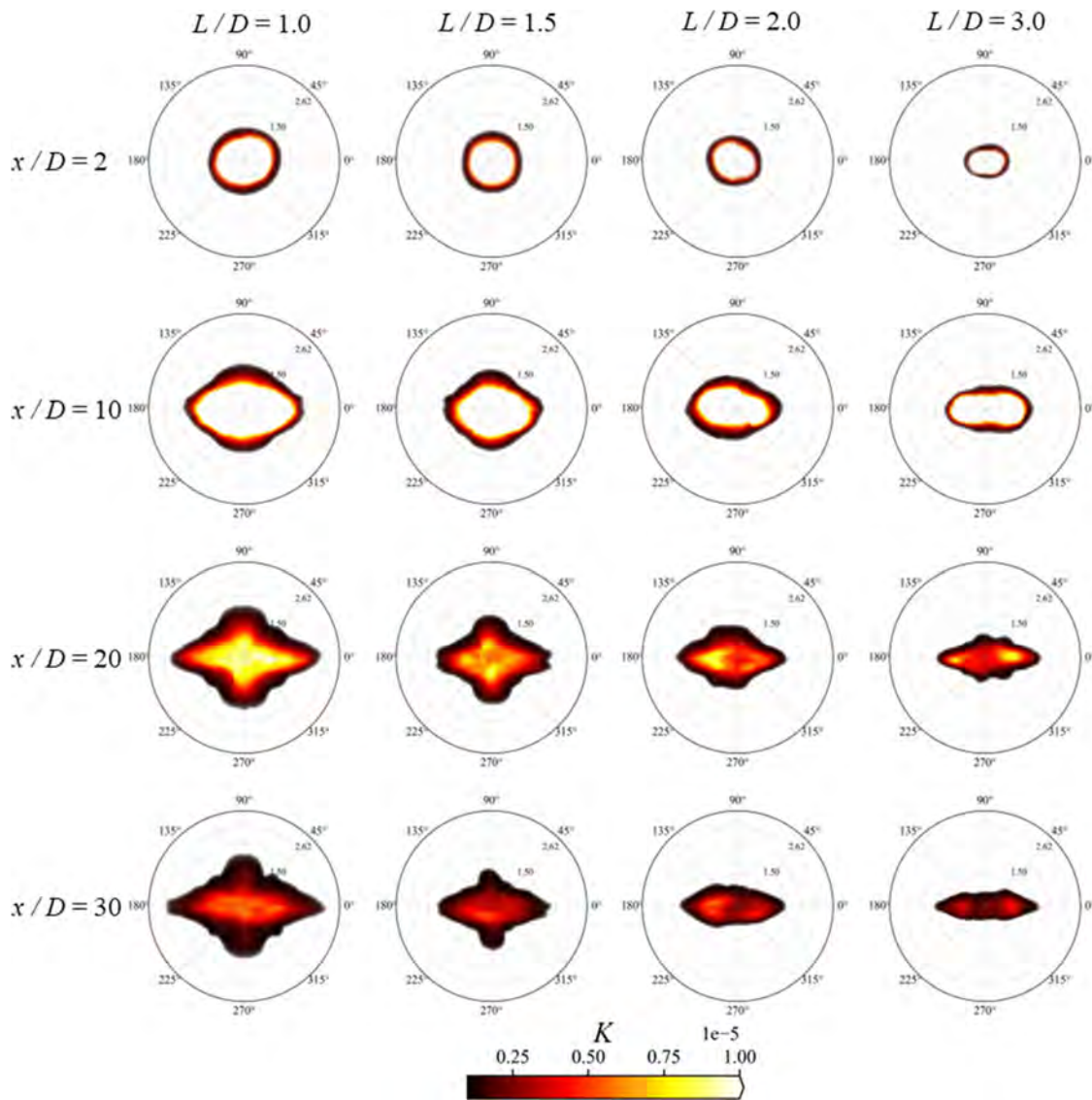
FIG. 19. Turbulent kinetic energy distribution at different aspect ratios and wake positions.

As the aspect ratio increases, all terms decrease in magnitude. Within the range $0.4 < x/D < 10$, the dissipation term remains consistently negative across different aspect ratios, while the transport term dominates. This behavior contrasts with the dominance of production observed in Pal et al.[44] It is important to note that, for method validation, the diameter of the prolate spheroid, the vertical density distribution, and the computational domain size used in the numerical simulations are based on the experimental setups of Bonnie and Eiff[12] and Lin et al.[6] The diameter of prolate spheroid, on the order of centimeters, necessitated a relatively small computational domain. The small size of the prolate spheroid results in a smaller wake region and a more compact turbulent structure. Consequently, the turbulent energy generation process occurs relatively quickly, leading to rapid diffusion and downstream transport of turbulent energy in the near-wake region. In this region, transport dominates production. Additionally, at different aspect ratios, the transport exhibits local minimum, with the location of local minimum shifting upstream as the aspect ratio increases.

V. CONCLUSIONS

This study employs large eddy simulation and the Boussinesq approximation to investigate the characteristics of wakes generated by prolate spheroid with different aspect ratios in a linear stratified flow, with an emphasis on the transition from blunt to streamlined geometries. The research primarily
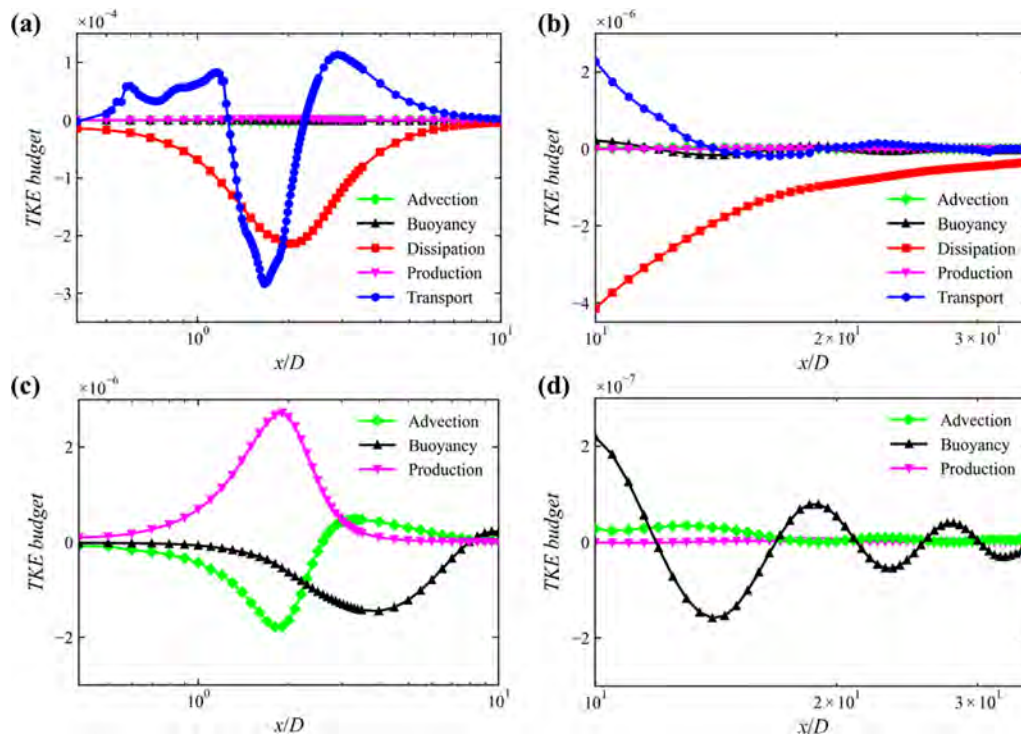
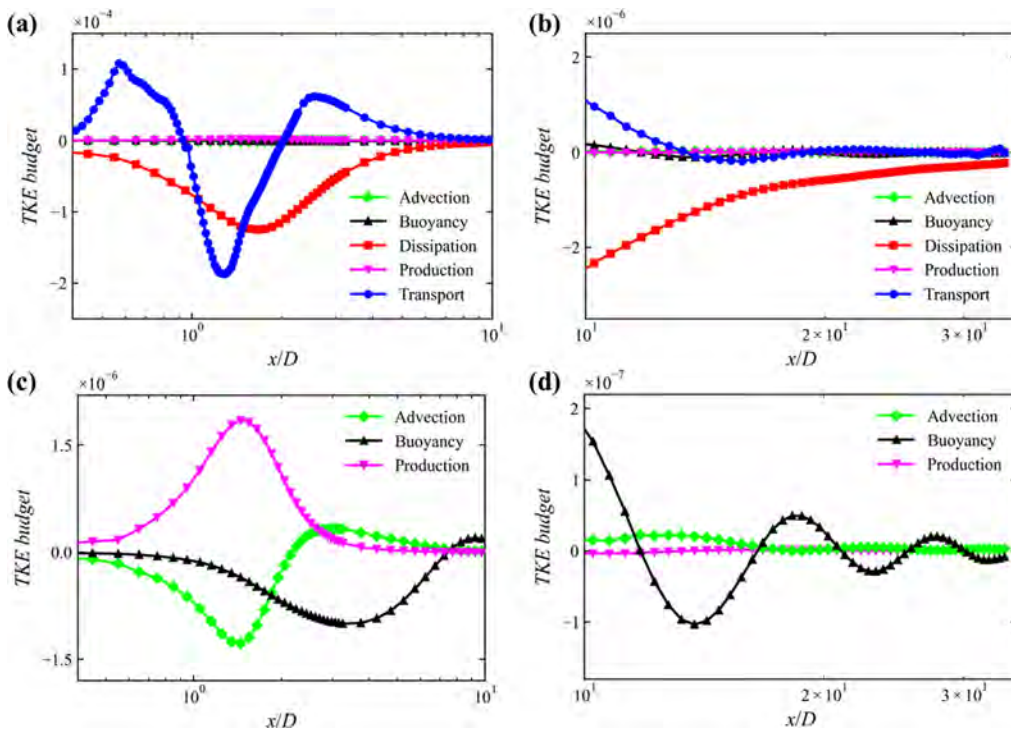**FIG. 20.** Terms in the turbulent kinetic energy budget ($L/D = 1.0$).

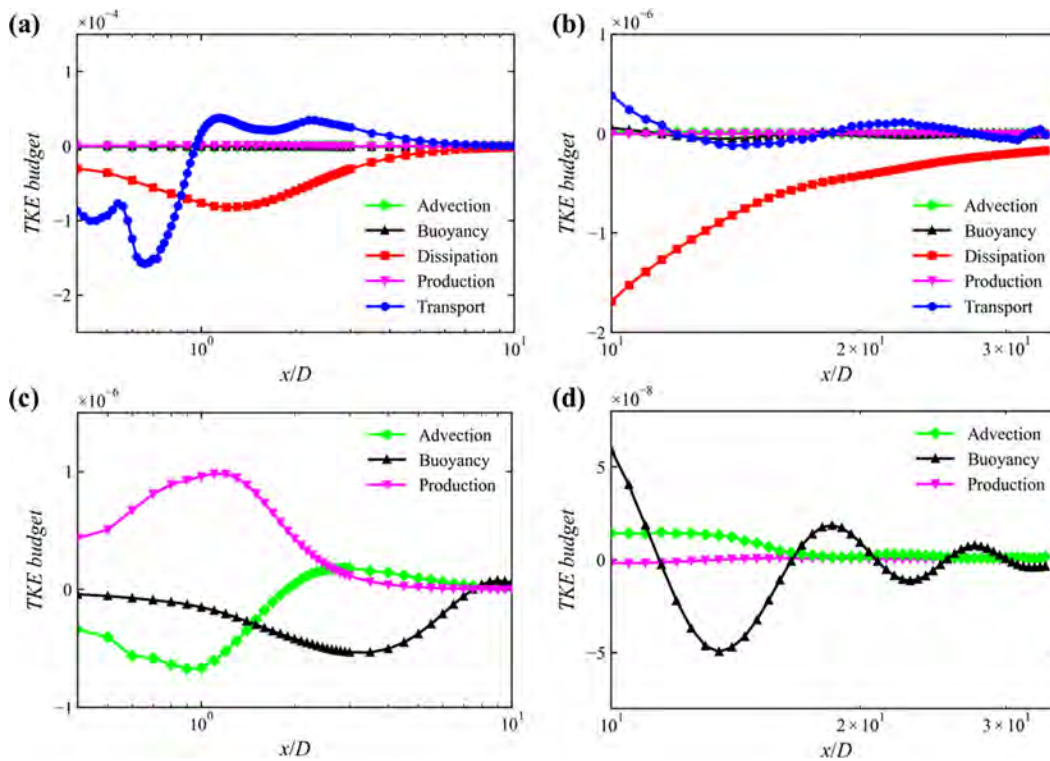**FIG. 21.** Terms in the turbulent kinetic energy budget ($L/D = 1.5$).

FIG. 22. Terms in the turbulent kinetic energy budget ($L/D = 2.0$).

focuses on the effects of different aspect ratios on defect velocity, wake length scales, root mean square (RMS) values of velocity components, power spectra, wake energy, and turbulent kinetic energy. These results contribute to the understanding of wake dynamics in stratified flows and provide a foundation for future studies on slender-body geometries. The conclusions are as follows:

As the aspect ratio increases, the starting and ending positions of the accelerated collapse stage progressively shift upstream, resulting in a shorter mean lifespan of the wake. The defect velocity along the wake centerline follows the relationships: $u \sim (x/D)^{-0.08}$ ($L/D = 1.0$), $u \sim (x/D)^{-0.09}$ ($L/D = 1.5$), $u \sim (x/D)^{-0.13}$ ($L/D = 2.0$), and $u \sim (x/D)^{-0.24}$ ($L/D = 3.0$), for $L/D = n$, the defect velocity satisfies $u \sim (x/D)^{(-0.0327n^2 + 0.0498n - 0.0955)}$.

As the aspect ratio increases, the half-width, half-height, the ratio of half-height to half-width, and the area of wake all decrease. The position of the recirculation zone significantly influences the half-width of the wake but has a relatively smaller impact on the half-height. After the starting position of the accelerated collapse stage, the half-width, half-height, the ratio of half-height to half-width, and the influence area of the wake oscillate periodically. These oscillations exhibit valleys at 1.5 buoyancy periods ($Nt = 3\pi$).

As the aspect ratio increases, root mean square (RMS) values of velocity components decrease. The vertical velocity and density are strongly influenced by buoyancy, undergoing periodic oscillations after the starting position of the accelerated collapse stage.

The oscillation wavelength corresponds to half a buoyancy period (πFr). As the aspect ratio increases, the Reynolds stress gradually decreases in magnitude and becomes concentrated near the centerline of the wake.

As the aspect ratio increases, the energy of wake decrease, the total energy, turbulent kinetic energy, and turbulent potential energy oscillate periodically, with the oscillation positions corresponding to half a buoyancy period (πFr). The turbulent kinetic energy for different aspect ratios follows the relationship TKE $\sim (x/D)^{-1.19}$. Additionally, as the aspect ratio increases, the mixing efficiency gradually improves.

As the aspect ratio increases, the spatial anisotropy of the turbulent energy distribution becomes more pronounced. In the turbulent kinetic energy budget, transport dominates. Within the range $10 < x/D < 35$, transport, advection, and buoyancy exhibit periodic oscillations, with the oscillation wavelength corresponding to half a buoyancy period (πFr).

It is important to note that the empirical formulas derived in this study are based on simulations conducted for blunt-body geometries ($L/D \leq 3.0$), when $L/D > 3.0$, may indicate significant deviations in wake behavior, suggesting a transition from blunt-body to slender-body flow regimes. This transition likely results in changes to flow separation, vortex shedding, and wake stability, which warrants further investigation. Determining the critical aspect ratio at which this transition occurs and analyzing the wake dynamics in slender-body regimes will be an important direction for future research.
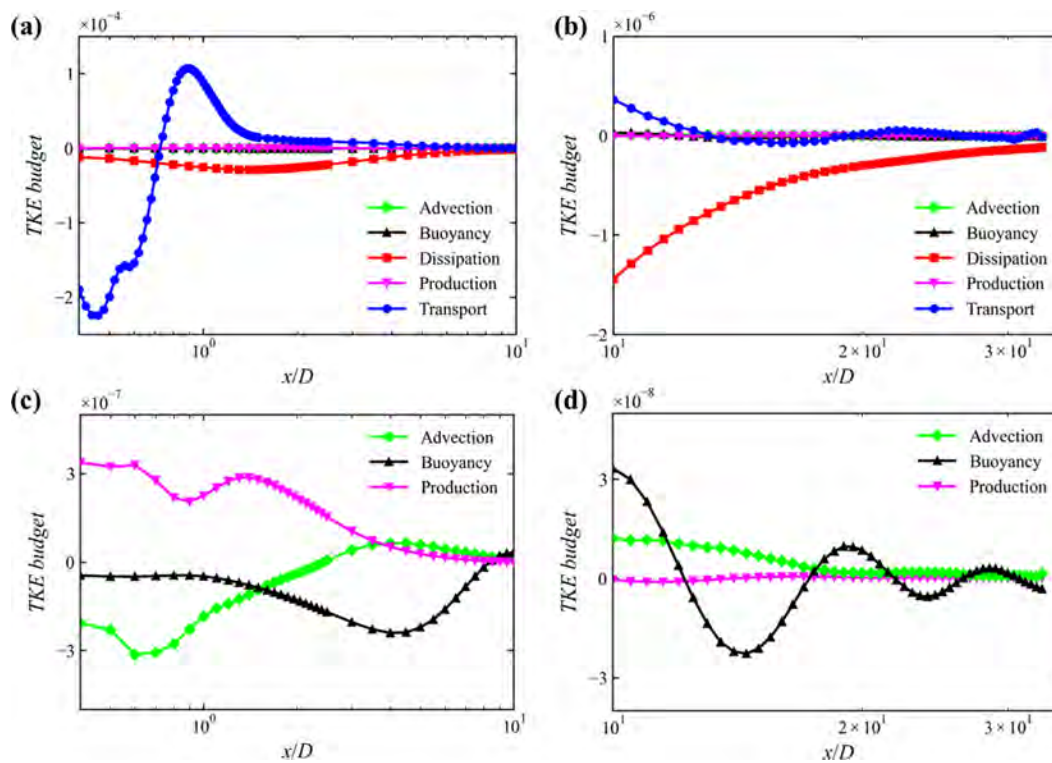
25 February 2025 14:59:01

FIG. 23. Terms in the turbulent kinetic energy budget ($L/D = 3.0$).

AUTHOR DECLARATIONS

Conflict of Interest

The authors have no conflicts to disclose.

Author Contributions

Gang Gao: Data curation (equal); Formal analysis (equal); Investigation (equal); Methodology (equal); Writing – original draft (equal). **Yangjun Wang:** Formal analysis (equal); Investigation (equal); Methodology (equal). **Kefeng Liu:** Data curation (equal); Investigation (equal); Methodology (equal). **Liushuai Cao:** Conceptualization (equal); Funding acquisition (equal); Project administration (equal); Supervision (equal); Writing – review & editing (equal). **Decheng Wan:** Funding acquisition (equal); Project administration (equal); Supervision (equal).

DATA AVAILABILITY

The data that support the findings of this study are available from the corresponding author upon reasonable request.

REFERENCES

[1]L. Cao, G. Gao, E. Guo, and D. Wan, "Hydrodynamic performances and wakes induced by a generic submarine operating near the free surface in continuously stratified fluid," J. Hydrodyn. **35**(3), 396–406 (2023).

[2]L. Cao, Y. Pan, G. Gao, L. Li, and D. Wan, "Review on the hydro- and thermodynamic wakes of underwater vehicles in linearly stratified fluid," J. Mar. Sci. Eng. **12**, 490 (2024).

[3]A. Poisson, C. Brunet, and J. C. Brun-Cottan, "Density of standard seawater solutions at atmospheric pressure," Deep-Sea Res. Pt. I **27**(12), 1013–1028 (1980).

[4]F. J. Millero and A. Poisson, "International one-atmosphere equation of state of seawater," Deep-Sea Res. Pt. I **28**(6), 625–629 (1981).

[5]H. J. Kim and P. A. Durbin, "Observations of the frequencies in a sphere wake and of drag increase by acoustic excitation," Phys. Fluids **31**(11), 3260–3265 (1988).

[6]Q. Lin, D. L. Boyer, and H. J. S. Fernando, "Turbulent wakes of linearly stratified flow past a sphere," Phys. Fluids A Fluid Dyn. **4**(8), 1687–1696 (1992).

[7]Q. Lin, W. R. Lindberg, D. L. Boyer, and H. J. S. Fernando, "Stratified flow past a sphere," J. Fluid Mech. **240**(1), 315 (1992).

[8]P. Bonneton, J. M. Chomaz, and E. J. Hopfinger, "Internal waves produced by the turbulent wake of a sphere moving horizontally in a stratified fluid," J. Fluid Mech. **254**, 23–40 (1993).

[9]J. M. Chomaz, P. Bonneton, and E. J. Hopfinger, "The structure of the near wake of a sphere moving horizontally in a stratified fluid," J. Fluid Mech. **254**, 1–21 (1993).

[10]G. R. Spedding, "The evolution of initially turbulent bluff-body wakes at high internal Froude number," J. Fluid Mech. **337**, 283–301 (1997).

[11]G. R. Spedding, F. K. Browand, and A. M. Fincham, "Turbulence, similarity scaling and vortex geometry in the wake of a towed sphere in a stably stratified fluid," J. Fluid Mech. **314**, 53–103 (1996).

[12]M. Bonnier and O. Eiff, "Experimental investigation of the collapse of a turbulent wake in a stably stratified fluid," Phys. Fluids **14**(2), 791–801 (2002).

[13]X. Xiang, T. J. Madison, P. Sellappan, and G. R. Spedding, "The turbulent wake of a towed grid in a stratified fluid," J. Fluid Mech. **775**, 149–177 (2015).

[14]Q. Chen, Q. Lin, Y. Xuan, and Y. Han, "Investigation on the thermohaline structure of the stratified wake generated by a propagating submarine," Int. J. Heat Mass Transfer **166**, 120808 (2021).

[15]W. Ma, Y. Li, Y. Ding, K. Hu, and L. Lan, "Numerical Simulations of Linearly Stratified Flow Past Submerged Bodies," Pol. Marit. Res **25**(s3), 68–77 (2018).

[16]F. Huang, Q. Meng, L. Cao, and D. Wan, "Wakes and free surface signatures of a generic submarine in the homogeneous and linearly stratified fluid," Ocean Eng. **250**, 111062 (2022).

[17]C.-A. Wang, D. Xu, J.-P. Gao, J.-Y. Tan, and Z.-Q. Zhou, "Numerical study of surface thermal signatures of lee waves excited by moving underwater sphere at low Froude number," Ocean Eng. **235**, 109314 (2021).

[18]C.-A. Wang, H. Zhang, and H.-L. Zhu, "Numerical predictions of internal waves and surface thermal signatures by underwater vehicles in density-stratified water using OpenFOAM," Ocean Eng. **272**, 113847 (2023).

[19]E. Nadaf, J. M. Brown, and T. Radko, "Turbulent wakes in a non-uniformly stratified environment," Phys. Fluids **34**(10), 105123 (2022).

[20]C. T. Jacobs, "Modelling a Moving Propeller System in a Stratified Fluid Using OpenFOAM," Fluids **5**(4), 217 (2020).

[21]M. B. De Stadler, S. Sarkar, and K. A. Brucker, "Effect of the Prandtl number on a stratified turbulent wake," Phys. Fluids **22**(9), 095102 (2010).

[22]P. J. Diamessis, G. R. Spedding, and J. A. Domaradzki, "Similarity scaling and vorticity structure in high-Reynolds-number stably stratified turbulent wakes," J. Fluid Mech. **671**, 52–95 (2011).

[23]K. A. Brucker and S. Sarkar, "A comparative study of self-propelled and towed wakes in a stratified fluid," J. Fluid Mech. **652**, 373–404 (2010).

[24]A. Pal, S. Sarkar, A. Posa, and E. Balaras, "Regeneration of turbulent fluctuations in low-Froude-number flow over a sphere at a Reynolds number of 3700," J. Fluid Mech. **804**, R2 (2016).

[25]J. A. Redford, T. S. Lund, and G. N. Coleman, "A numerical study of a weakly stratified turbulent wake," J. Fluid Mech. **776**, 568–609 (2015).

[26]K. Chongsiripinyo, "The downstream of a density-stratified sphere wake," Eng. J. **25**(5), 1–12 (2021).

[27]K. Chongsiripinyo and S. Sarkar, "Stratified turbulence in disk wakes," Report No. 6 (Department of Mechanical and Aerospace Engineering, University of California at San Diego, La Jolla, CA, 2019).

[28]K. Chongsiripinyo and S. Sarkar, "Decay of turbulent wakes behind a disk in homogeneous and stratified fluids," J. Fluid Mech. **885**, A31 (2020).

[29]R. Pasquetti, "Temporal/spatial simulation of the stratified far wake of a sphere," Comput. Fluids **40**(1), 179–187 (2011).

[30]G. Gao, Y. Pan, Y. Wang, Z. Shen, L. Cao, and D. Wan, "Evolution and propagation characteristics of the wake induced by an underwater vehicle moving in two layers of fluid: A parametric study," Phys. Fluids **36**(11), 112125 (2024).

[31]J. L. Ortiz-Tarin, K. C. Chongsiripinyo, and S. Sarkar, "Stratified flow past a prolate spheroid," Phys. Rev. Fluids **4**(9), 094803 (2019).

[32]J. L. Ortiz-Tarin, S. Nidhan, and S. Sarkar, "The high-Reynolds-number stratified wake of a slender body and its comparison with a bluff-body wake," J. Fluid Mech. **957**, A7 (2023).

[33]C.-Y. Ohh and G. R. Spedding, "The effects of stratification on the near wake of 6:1 prolate spheroid," J. Fluid Mech. **997**, A43 (2024).

[34]K. Chongsiripinyo, A. Pal, and S. Sarkar, "On the vortex dynamics of flow past a sphere at Re = 3700 in a uniformly stratified fluid," Phys. Fluids **29**(2), 020704 (2017).

[35]T. S. Orr, J. A. Domaradzki, G. R. Spedding, and G. S. Constantinescu, "Numerical simulations of the near wake of a sphere moving in a steady, horizontal motion through a linearly stratified fluid at Re = 1000," Phys. Fluids **27**(3), 035113 (2015).

[36]Q. Zhou, "Mixing in a strongly stratified turbulent wake quantified by bulk and conditional statistics," J. Fluid Mech. **997**, A41 (2024).

[37]A. VanDine, H. T. Pham, and S. Sarkar, "Turbulent shear layers in a uniformly stratified background: DNS at high Reynolds number," J. Fluid Mech. **916**, A42 (2021).

[38]R. V. More and A. M. Ardekani, "Motion in Stratified Fluids," Annu. Rev. Fluid Mech. **55**(1), 157–192 (2023).

[39]R. Dandekar, V. A. Shaik, and A. M. Ardekani, "Motion of an arbitrarily shaped particle in a density stratified fluid," J. Fluid Mech. **890**, A16 (2020).

[40]R. Dandekar and A. M. Ardekani, "Swimming sheet in a viscosity-stratified fluid," J. Fluid Mech. **895**, R2 (2020).

[41]Siemens Digital Industries Software, "Simcenter STAR-CCM+ user guide, version 2302" (2023).

[42]I. Rodriguez, R. Borell, O. Lehmkuhl, C. D. P. Segarra, and A. Oliva, "Direct numerical simulation of the flow over a sphere at Re = 3700," J. Fluid Mech. **679**, 263–287 (2011).

[43]V. Seidl, S. Muzaferija, and M. Perić, "Parallel DNS with local grid refinement," Appl. Sci. Res. **59**, 379–394 (1997).

[44]A. Pal, S. Sarkar, A. Posa, and E. Balaras, "Direct numerical simulation of stratified flow past a sphere at a subcritical Reynolds number of 3700 and moderate Froude number," J. Fluid Mech. **826**, 5–31 (2017).

[45]G. Constantinescu and K. Squires, "Numerical investigations of flow over a sphere in the subcritical and supercritical regimes," Phys. Fluids **16**(5), 1449–1466 (2004).

[46]P. Meunier and G. R. Spedding, "Stratified propelled wakes," J. Fluid Mech. **552**, 229–256 (2006).

[47]C. E. Itsweire, J. R. Koseff, D. A. Briggs, and J. H. Ferziger, "Turbulence in stratified shear flows: Implications for interpreting shear-induced mixing in the ocean," J. Phys. Oceanogr. **23**, 1508 (1993).

25 February 2025 14:59:01